

Cyclic Fatigue of Rocks and Concrete

Author: M. Sc. Zhengyang Song & Prof. Dr. habil. Heinz Konietzky
(TU Bergakademie Freiberg, Geotechnical Institute)

1. Introduction	2
1.1 What is fatigue?	2
1.2 Classification of fatigue	2
1.2.1 Classification based on frequency	3
1.2.2 Classification based on loading scheme.....	3
1.2.3 Classification based on stress state	4
1.2.4 Classification based on fatigue life	4
2. Basic fatigue experimental concepts	4
2.1 Dynamic loading and fatigue (cyclic) loading	4
2.2 Types of fatigue experiments	5
2.2.1 Compressive fatigue tests	5
2.2.2 Tensile fatigue tests.....	6
2.2.3 Shear fatigue tests.....	7
2.2.4 Torsional fatigue tests	8
2.2.5 Flexural fatigue tests	8
2.2.6 Static fatigue tests	8
2.2.7 Freezing-thawing cyclic tests.....	9
2.2.8 Wetting-drying cyclic tests	9
3. Example: compressive cyclic loading of concrete samples	11
3.1 Fatigue testing set-up.....	11
3.2 Characteristics of dissipated energy	15
3.2.1 Effect of maximum cyclic load level on energy dissipation	17
3.2.2 Effect of minimum cyclic load level on energy dissipation	22
3.3 P-wave speed evolution and AE characteristics	23
3.4 Failure patterns of concrete specimens	34
4 References	36

1. Introduction

1.1 What is fatigue?

Fatigue is a common mechanical behaviour in nature and engineering. Many environmental and human-induced loadings are cyclic. Currently, the most general definition of *fatigue* refers to the weakening and deterioration of materials when exposed to repetitive loading. Fig. 1.1 briefly illustrates the history of fatigue research and documents some important milestones and researchers who have made major contributions to fatigue investigations. The fatigue behaviour was first scientifically reported by the German mining engineer Albert (1838). He found the conveyor chains used in the mine can easily fail even if the external load is much smaller than the material strength (Schütz 1996). The German railway engineer August Wöhler put the fatigue research on a higher level by introducing the S-N curve (also known as Wöhler curve). This was the first quantitative characterization of the relation between fatigue life and applied loads (Wöhler 1870). Nowadays, the S-N curve is still an important reference for production standards in construction and material sciences. The Paris' law was proposed by Paris et al. (1963) to relate the stress intensity factor to sub-critical crack growth under a fatigue stress regime. This equation is still the most popular crack growth criterion for fatigue loading. At present, the fatigue research is not only limited to metal and alloy materials, geo- and bio-materials also have a risk of fatigue failure.

1.2 Classification of fatigue

Based on chosen parameters, different fatigue classifications exist. Here, only the classification schemes based on frequency, loading scheme, stress state and fatigue life will be presented.

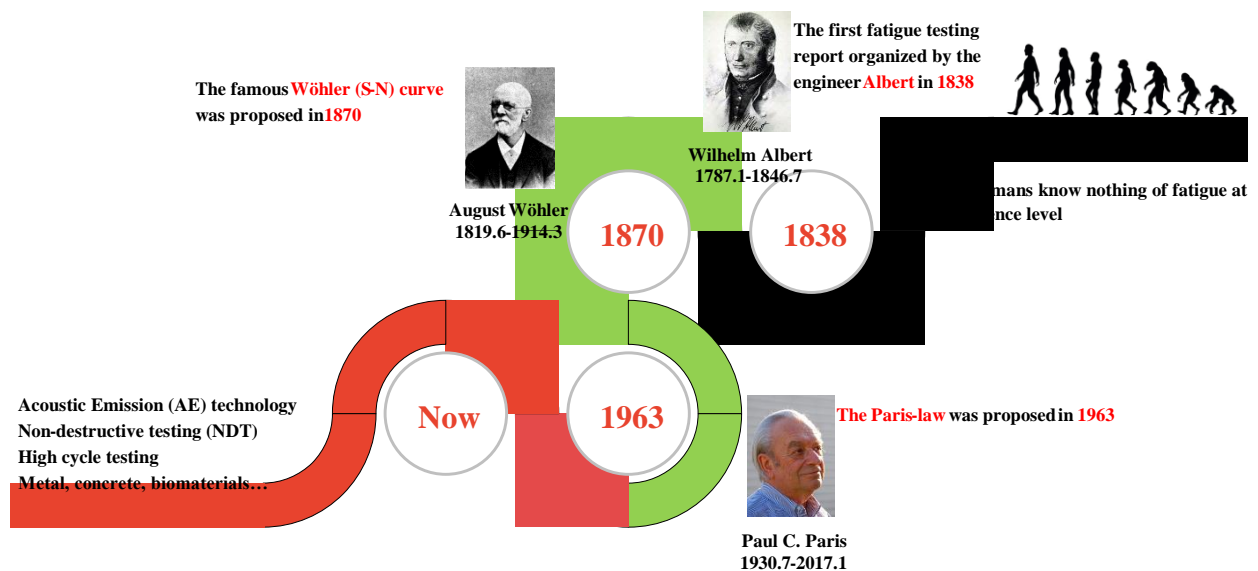


Fig. 1.1: History of fatigue research incl. important milestones and researchers

1.2.1 Classification based on frequency

According to the different cyclic loading frequencies, the fatigue can be categorised as follows (Xu 2016, see Fig. 1.2):

- High frequency fatigue (frequency > 10 Hz)
- Medium frequency fatigue (10 Hz > frequency > 0.1 Hz)
- Low frequency fatigue (frequency < 0.1 Hz)
- Static fatigue (constant load)

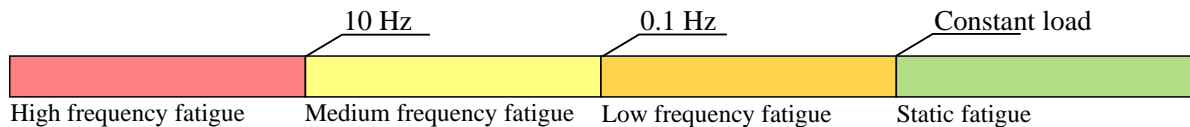


Fig. 1.2: Fatigue classification based on loading frequency

1.2.2 Classification based on loading scheme

According to the loading scheme, fatigue can be categorised as follows:

- Strain-controlled fatigue
- Stress-controlled fatigue.

In strain-controlled fatigue testing, the amplitude of strain during each cycle is constant, the elastic modulus will gradually reduce until failure, see Fig. 1.3a; in stress-controlled fatigue testing, the maximum and minimum load level of each cycle remain the same, the axial strain usually acts as a variable and evolves with loading time, the elastic modulus almost doesn't change when sample remains stable, see Fig. 1.3b.

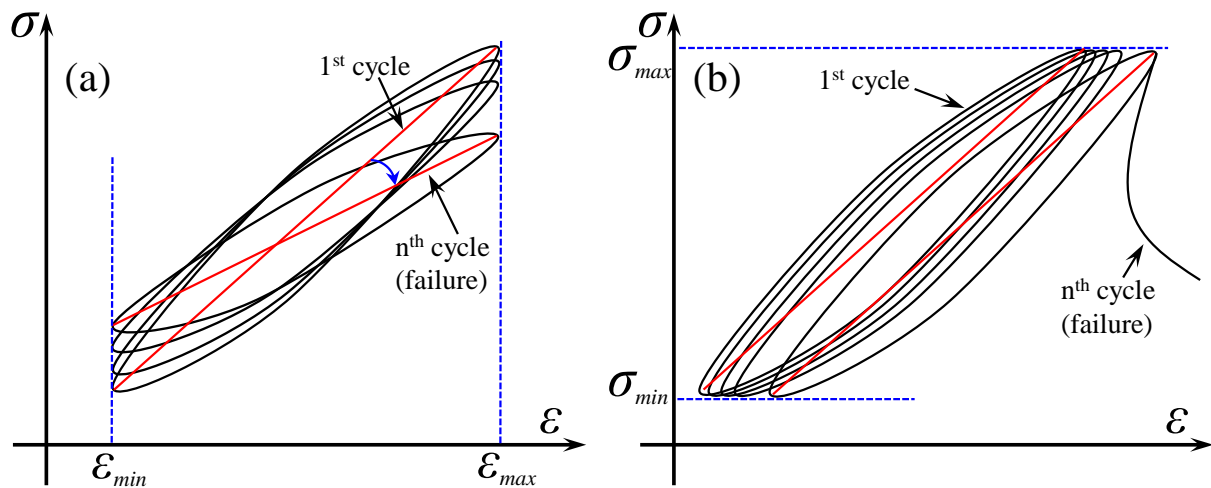


Fig. 1.3: Fatigue classification based on loading scheme (a) strain-controlled fatigue (b) stress-controlled fatigue

1.2.3 Classification based on stress state

Based on the stress state, the fatigue can be classified as follows:

- Uniaxial fatigue
- Multi-axial fatigue

The uniaxial fatigue is quite common in nature and engineering, such as bridge foundations, pavements and highways.

1.2.4 Classification based on fatigue life

Based on the number of cycles up to failure, the fatigue can be categorized as:

- High cycle fatigue (HCF)
- Low cycle fatigue (LCF).

10^4 cycles are always considered as limit for HCF, but there is no consensus about the limit value for LCF. The most obvious characteristic for LCF is that plastic deformation is quite large during each cycle. This indicates that LCF usually corresponds to a higher load level. Fig. 1.4 illustrates the range of fatigue life corresponding to different natural and human-induced activities. The crustal plate (earth) movement can lead to the most serious damage in quite short time. The aerospace-related materials usually have the most stringent requirements on fatigue life (larger than 10^8 cycles).

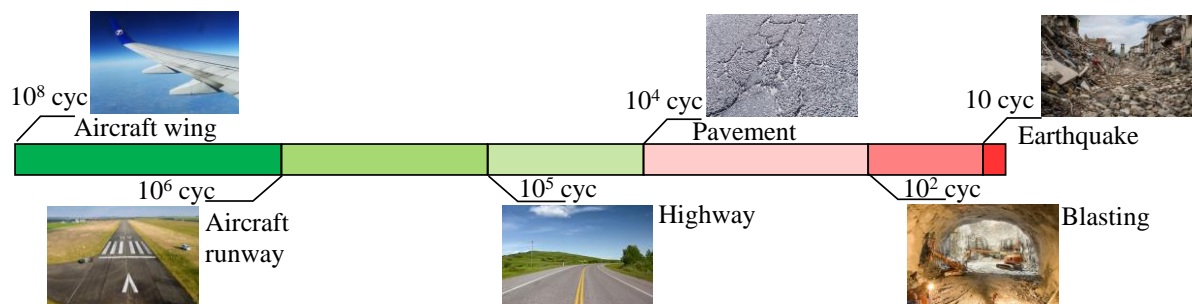


Fig. 1.4: Range of fatigue life of natural and human-induced activities

2. Basic fatigue experimental concepts

2.1 Dynamic loading and fatigue (cyclic) loading

The concepts of dynamic loading and fatigue loading are not equivalent, however, many incorrect usages of the two concepts in literature can lead to some confusion. For dynamic loading, the inertial forces generated inside the loaded sample are quite large compared to the loading force. On the contrary (for quasi-static loading), the inertial forces are almost negligible. Dynamic loading is commonly encountered with respect to shocks, blasting, high-speed trains, etc. If the loading rate is very high during experiments, waves propagate and their superposition produces a stress distribution different from the quasi-static situation.

Fatigue loading is characterised by an applied time-dependent (displacement, load) signal which exhibits a repetitive manner, in opposition to monotonic loading where applied load or deformation is continuously increasing. A cyclic load signal is the combination of a mean load, $\sigma_{\text{mean}}(t)$ and a cyclic amplitude $\Delta\sigma(t, T)$, where T is the period of the load wave, see Fig. 2.1a. Loading frequency is important because high frequencies

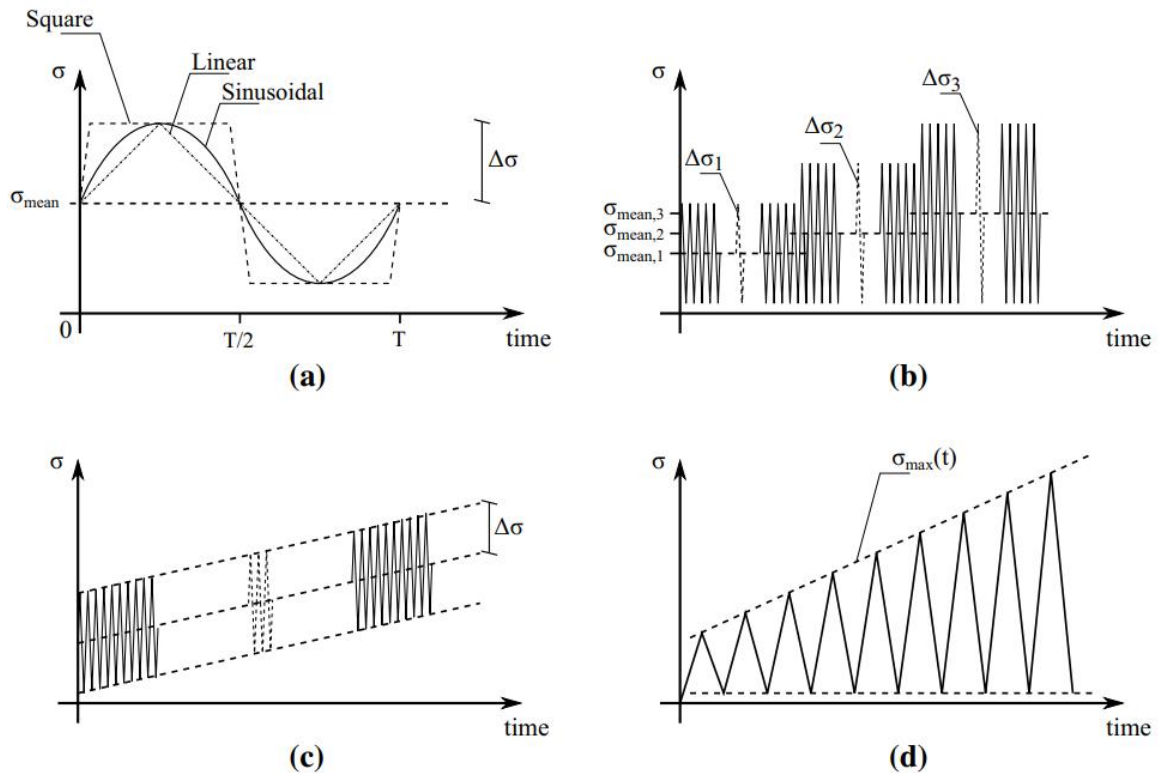


Fig. 2.1: (a) different types of signal (b) batch of constant amplitude signals (c) ramp signal (d) damage-controlled signal

are usually related to dynamic loading. The cyclic loading wave can have different shape as documented in Fig. 2.1a (Cerfontaine & Collin 2018). The most common cyclic loading wave forms are: square, triangle or sinusoidal. The sinusoidal signal is more close to the stress wave generated during rock bursts or earthquakes. It is proven on different materials that the shape of the signal affects the results. Square signal is the most damaging, while triangle waves are the least damaging (Bagde & Petroš 2005a; Erarslan et al. 2014). According to Cerfontaine & Collin (2018), the mean amplitude and the loading amplitude could be constant or changeable. Most of the tests found in literature consider constant amplitudes or increasing step by step as shown in Fig. 2.1b. The damage controlled test refers to the testing shown in Fig. 2.1d which adopts increasing mean and amplitude stress. The ramp signal, see Fig. 2.1c, is characterised by a constant amplitude but an increasing mean stress.

2.2 Types of fatigue experiments

2.2.1 Compressive fatigue tests

The uniaxial compressive fatigue test is a common and typical test especially for geo- and construction materials, such as rocks (Bagde & Petroš 2005b; Xiao et al. 2009; Liu et al. 2015; Jia et al. 2019; Li et al. 2019), soils (Leng et al. 2018; Oliveira et al. 2018), asphalt (Wang et al. 2017; Isailović & Wistuba 2018) and concrete (Lei et al. 2017; Hu et al. 2018; Song et al. 2018, 2019). This kind of test often corresponds to the actual stress condition of engineering structures exposed to one dimensional load, such as bridge foundations or pavements. This test is also a fundamental approach to obtain S-N curves. The triaxial compressive fatigue test is specifically designed for materials which are usually deeply buried in the underground, such as in mines, tunnels, or hydropower stations.

Under these conditions, the lateral strain of the material is usually confined and a pronounced triaxial state of stress develops. Many triaxial fatigue tests on brittle geo-materials (Liu et al. 2011; Liu & He 2012; Ma et al. 2013; Jia et al. 2018; Zhao et al. 2018) document, that with increased confining pressure residual axial and volumetric strain become larger. When the samples show dilatant behaviour, the corresponding axial strain is greater for cyclic loading than static triaxial loading.

2.2.2 Tensile fatigue tests

For geo-materials, the direct tensile fatigue test is not that often used due to the difficulties in sample preparation, but in the last years, more and more direct tensile fatigue tests are carried out (Reinhardt & Cornelissen 1984; Fan et al. 2016; Chen et al. 2017). Fig 2.2 shows a typical direct tensile fatigue test by using concrete material. In this test (Chen et al. 2017), two cylindrical discs (steel plates) are pasted with the ends of the specimen by a structural adhesive. The other sides of the discs are connected to the test device by spherical hinges and screws. The spherical hinges reduce the eccentricity. The device stretches the plates and then the force is transmitted to the specimen.

Considering the difficulties with device operation and sample preparation in direct tensile fatigue tests, indirect methods like the Brazilian test (Vicentini et al. 2014; Liu et al. 2018) are becoming popular. According to the ISRM suggested methods (ISRM 1978), a thin circular-shaped disc is vertically compressed in the diametrical direction, which leads to tensile failure. Theoretically, the tensile failure should be initiated at the central point of the disc where the tensile stress has the maximum value. However in laboratory tests, sometimes the crack initiates at the contact between loading platens and sample due to stress concentrations (Fairhurst 1964; Hudson et al. 1972; Swab et al. 2011). Some efforts have been made to ensure a reasonable failure mode of the tested discs. These modifications are:

- change of the shape of loading platen, see Fig. 2.3 (Li & Wong 2013)
- change of Brazilian disc shape, see Fig. 2.4 (Wang & Xing 1999; Wang et al. 2004).

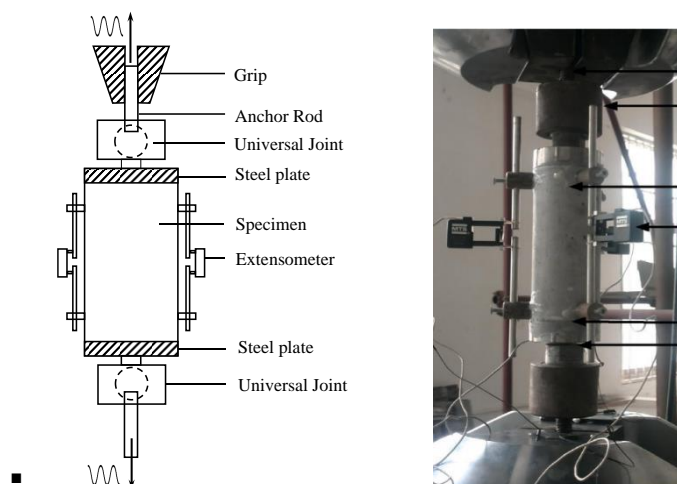


Fig 2.2: Direct tensile fatigue test: scheme and experimental setup (Chen et al. 2017)

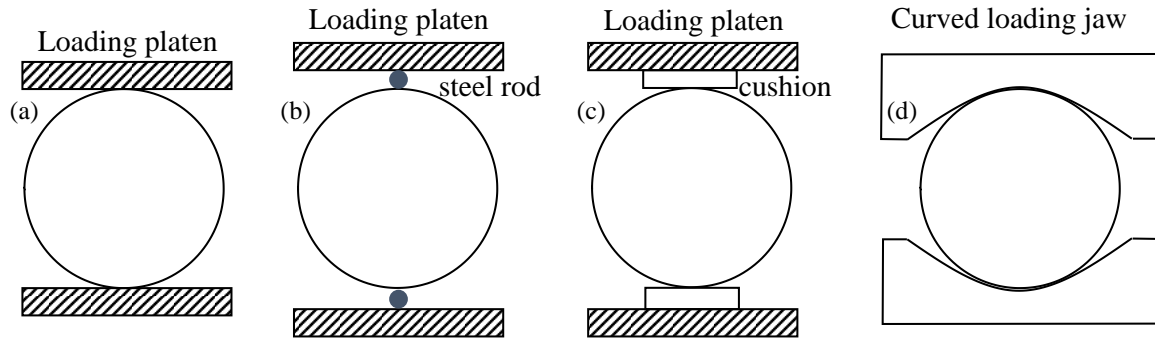


Fig. 2.3 Typical Brazilian tensile test loading configurations: (a) flat loading platens (b) flat loading platens with two small-diameter steel rods (c) flat loading platens with cushion and (d) curved loading jaws (Li & Wong 2013)

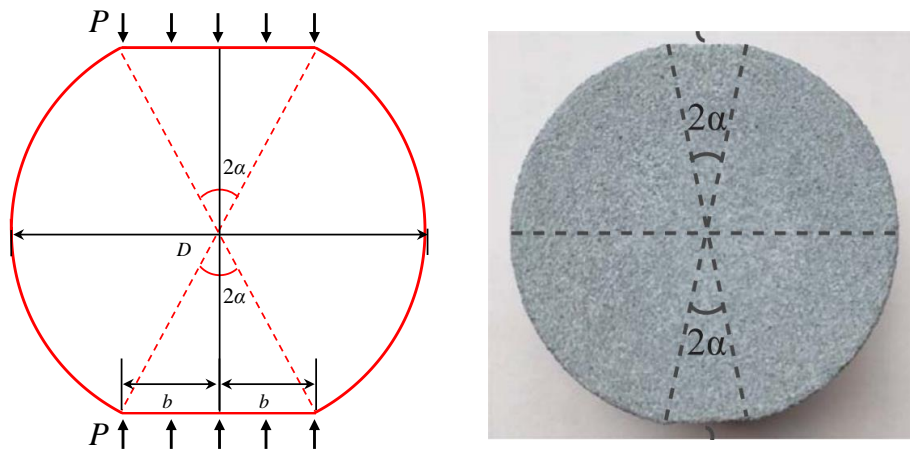


Fig. 2.4. Flattened Brazilian disc (FBD)(Liu et al. 2018)

2.2.3 Shear fatigue tests

Cyclic direct shear tests are often carried out on soils or clay materials (Boukpeti et al. 2014; Kim et al. 2015; Le & Ghayoomi 2017). During the tests, a vertical stress is usually applied on the sample and the cyclic shear stress is controlled by the movement of a tray which is activated by a hydraulically pressurized actuator. Besides cyclic direct shear tests on intact samples, also the cyclic shear fatigue of planar or rough joints can be investigated (Jing et al. 1993; Dang et al. 2016, 2017; Fathi et al. 2016) as shown in Fig. 2.5.

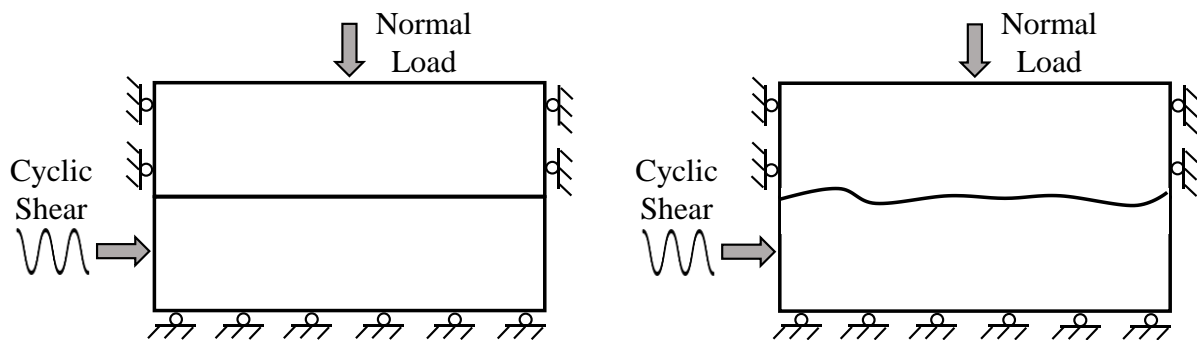


Fig. 2.5. Cyclic shear test of planar or natural joints

2.2.4 Torsional fatigue tests

During these tests, a force is applied to the sample via bending moments. The sample rotates so that each surface experiences alternating tensile and compressive stresses. However, due to the difficulties of sample preparation, this kind of test is usually only used to test metal materials (Bernard et al. 2011; Minto et al. 2017; Özdeş et al. 2017) or ceramics (Yassini et al. 2016).

2.2.5 Flexural fatigue tests

In the flexural test, also known as three-point or four-point flexural (bending) test, the specimen always has either a semi-circular or rectangular cross-section and is cyclically bent until macroscopic fractures appear and failure happens, see Fig. 2.6. The flexural property is an important factor in design of pavements and railways. The detailed procedure in respect to flexural tests with geo-materials is discussed by Singh & Kaushik (2003); Ramakrishnan et al. (2005); Singh & Sharma (2007); Goel et al. (2012); Tarefder et al. (2013); Hanif et al. (2018) and Soheli et al. (2018).

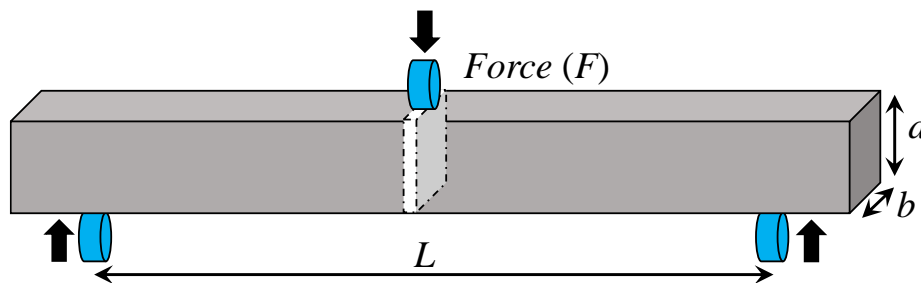


Fig. 2.6 Three-point flexure test on rectangular samples

2.2.6 Static fatigue tests

The static fatigue is related to “delayed fracture”, referring to the time-dependent behaviour under constant load, e.g. (Chen & Konietzky 2014; Xu et al. 2018). Static fatigue is associated with stress corrosion and creep behaviour. Systematic static fatigue tests were performed for example with Lac du Bonnet granite (Schmidtke & Lajtai 1985), see Fig. 2.7. The diagram shows the stress-ratio (ratio of applied stress to UCS) vs. lifetime (duration up to failure).

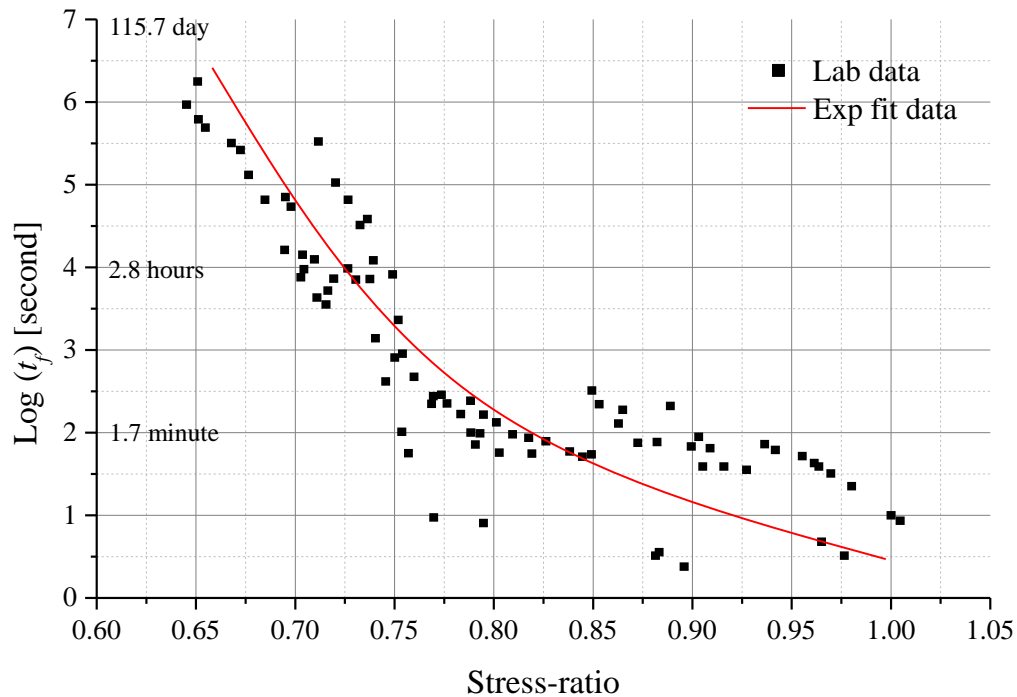


Fig. 2.7: Static fatigue lab test of Lac du bonnet granite: lifetime vs. stress ratio (Schmidtke & Lajtai 1985)

2.2.7 Freezing-thawing cyclic tests

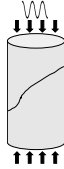
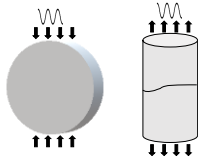
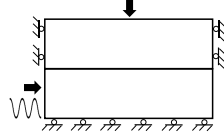
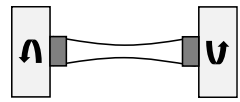
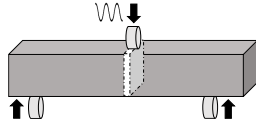
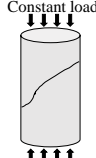
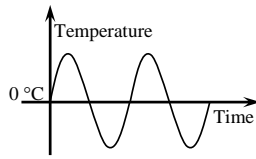
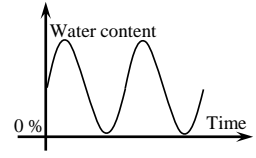
Freezing-thawing cyclic (fatigue) tests aim to explore the effect of cyclic temperature variations (above and below 0 °C) on partial or fully saturated materials. Water expands up to about 9% of its original volume when frozen. This expansion induces tensile stresses and damages the micro structure. When material is thawed, water flows through the fractured micro pores which can also increase the damage (Chen et al. 2004; Zhang et al. 2004; Grossi et al. 2007). These effects are of special importance for geo-materials in cold regions, such as soils (Qi et al. 2006; Wang et al. 2007), rocks (Tan et al. 2011) and concretes (Polder & Peelen 2002; Bumanis et al. 2018). During freezing-thawing tests, the samples are stored in temperature and humidity controlled containers undergoing the cyclic change of temperature. Compared to the mechanical fatigue tests, the duration of one cycle in freeze-thaw fatigue tests is much longer and can last 4 - 10 hours (Tan et al. 2011). After cyclic freezing-thawing treatment mechanical testing follows. Literature reviews about this topic are provided by Aïtcin (2003), Qi et al. (2006) and Henry (2007).

2.2.8 Wetting-drying cyclic tests

The wetting-drying cyclic tests mainly aim to investigate the influence of cyclic change of water content in geo-materials. Wetting and drying leads to changes of properties, including bulk density, weight loss, water absorption (water content), effective porosity and P-wave velocity (Sumner and Loubser 2008; Özbek 2014; Khanlari and Abdilor 2015; Xu et al. 2017). A wetting-drying cycle is generally divided into two phases: saturation (from dry to saturated state) and drying (from saturated to dry state). In each cycle, specimens were submerged into water or other fluids for a given time to reach the saturated state at a constant temperature, and then taken out and getting air-dried at the same temperature (Zhou et al. 2017). After cyclic wetting-drying treatment, the samples experience mechanical testing.

A brief comparison of the eight types of fatigue tests are presented in Table 2.1, each type corresponds to different kind of engineering problems.

Tab. 2.1: Comparison between different fatigue tests

Types of fatigue tests	Fatigue reasons	Common test materials	Test schemes	Corresponding engineering problems
Compressive fatigue tests	Stress induced failure	Rock, Concrete, Soil, Laminate, Asphalt		<ol style="list-style-type: none"> 1. Railway 2. Pavement 3. Foundation 4. Mining 5. ...
Tensile fatigue tests	Stress induced failure	<ol style="list-style-type: none"> 1. Direct tensile test: Metal, Alloy, Concrete 2. Brazilian test: Rock, Concrete 		<ol style="list-style-type: none"> 1. Crane 2. Bridge 3. Truss 4. Concrete beam 5. ...
Shear fatigue tests	Stress induced failure	Metal, Soil, Rock, Concrete		<ol style="list-style-type: none"> 1. Slope 2. Engineering geology 3. Airplane wing 4. ...
Torsional fatigue tests	Stress induced failure	Metal, Alloy, Ceramics		<ol style="list-style-type: none"> 1. Windmill 2. Turbine 3. Engine shaft 4. ...
Flexural fatigue tests	Stress induced failure	Rock, Concrete, Laminate, Metal		<ol style="list-style-type: none"> 1. Offshore structures 2. Pavement 3. Bridge deck 4. ...
Static fatigue tests	Stress induced failure	Rock, Concrete		<ol style="list-style-type: none"> 1. Gas cavern 2. Dam 3. Hydro station 4. ...
Freezing-thawing tests	Water/temp. effect	Rock, Concrete, Soil		<ol style="list-style-type: none"> 1. Cold region construction 2. Aerospace material 3. ...
Wetting-drying tests	Water effect	Rock, Concrete, Soil		<ol style="list-style-type: none"> 1. Highway 2. Natural rock and soil 3. ...

3. Example: compressive cyclic loading of concrete samples

3.1 Fatigue testing set-up

The specimens (125 mm height (H) and 50 mm diameter (ϕ)) are made of plain concrete of type C25/30 XC4 XF1. The specimens are produced in two series (S1 and S2) according to the production date, see Fig. 3.1. Before fatigue testing, ultrasonic wave speed and dynamic elastic modulus were measured to evaluate magnitude and scatter of the physical properties, see Fig. 3.2. The specimen properties are presented in Table 3.1. S1-1 indicates the sample No. #1 in series 1 and so on. S1-4 and S1-9 are selected to measure the uniaxial compressive strength (UCS) representative for S1. S2-15 and S2-16 are selected to measure UCS representative for S2. The loading rate in UCS tests is 5 MPa/min for S1-4 and S1-9 and 0.125 mm/min for S2-15 and S2-16. In order to avoid early failure during the fatigue testing, the smaller reference values of 18.0 MPa and 19.0 MPa are adopted as UCS for S1 and S2 samples, respectively.

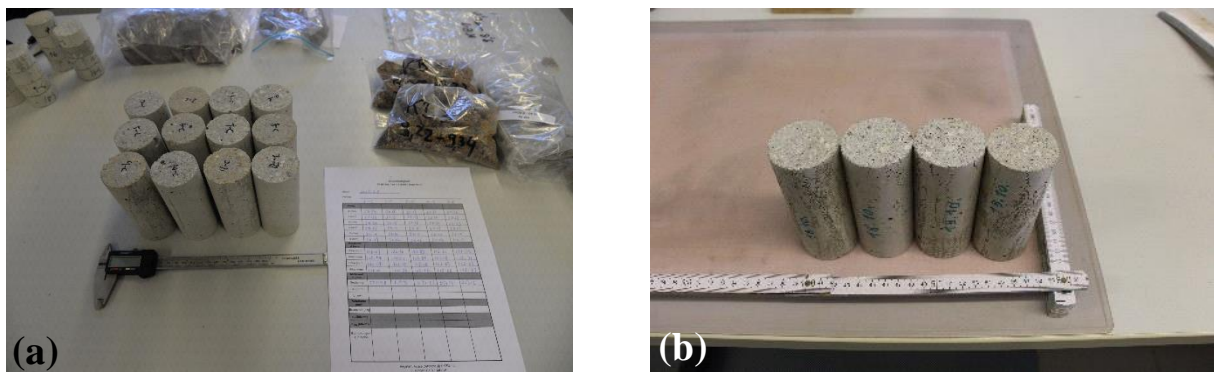


Fig. 3.1: Concrete samples (a) series 1 (b) series 2



Fig. 3.2: (a) ultrasonic wave speed measurement (b) data acquisition

Tab. 3.1: Properties of cyclically loaded concrete samples

Sample No.	Wave velocity [m/s]		Dynamic Young's modulus [GPa]	Length [mm]	Diameter [mm]	Density [g/cm ³]	UCS [MPa]
	P-wave	S-wave					
S1-1	3481	2129	22.86	125.31	50.14	2.10	
S1-2	3536	2196	23.99	126.07	50.21	2.10	
S1-3	3606	2229	24.88	125.60	50.21	2.10	
S1-4	3631	2272	25.81	125.88	50.06	2.13	18.04
S1-5	3657	2260	25.83	125.74	50.17	2.12	
S1-6	3674	2259	25.88	126.03	50.21	2.12	
S1-7	3730	2265	26.08	125.51	50.22	2.10	
S1-8	3731	2331	27.39	126.31	50.08	2.14	
S1-9	3774	2313	27.48	125.85	50.15	2.14	19.28
S1-10	3790	2432	29.52	125.76	50.14	2.17	
S1-11	3791	2274	27.00	125.66	50.21	2.14	
S1-12	3832	2459	30.11	126.09	50.18	2.17	
S2-13	4096	2289	28.75	123.74	50.31	2.16	
S2-14	4046	2323	28.63	123.70	50.45	2.11	
S2-15	4173	2416	31.75	123.46	50.31	2.18	21.01
S2-16	3760	2165	25.02	123.69	50.36	2.13	19.27

* The loading rate for S1-3, S1-4 is 5.00 MPa/min, for S2-15, S2-16 is 0.125 mm/min

The uniaxial compression testing was conducted with a MTS 20/M machine, see Fig. 3.3a. The loading frame stiffness of MTS 20/M is 5E8 N/m and the maximum load is 100 kN. The fatigue testing was carried out with TIRA 28500 test system illustrated in Fig. 3.3b. The system is able to perform both, static and dynamic compression tests. It has a compression capacity of 500 kN, with a piston stroke length of 1300 mm and a maximum loading velocity of 200 mm/min. The external measuring system which consists of vertical and radial strain measurement is shown in Fig. 3.3c. The axial deformation of the whole specimen l_w is measured directly through displacement of loading platen of the TIRA test system. The external axial strain measurement (ϵ_a) is performed by linear variable differential transformer (LVDT) located at the central part of the sample and has a measuring length l_m of 50 mm. Radial strain ϵ_r was measured through radial chain strain gauge also placed at the central part of the specimen. For the purpose of measuring the strains at different sections (top, middle and bottom) of the specimen, strain gauges are glued at the different parts of specimen surface to measure the axial and radial strain, see Fig. 3.3d.

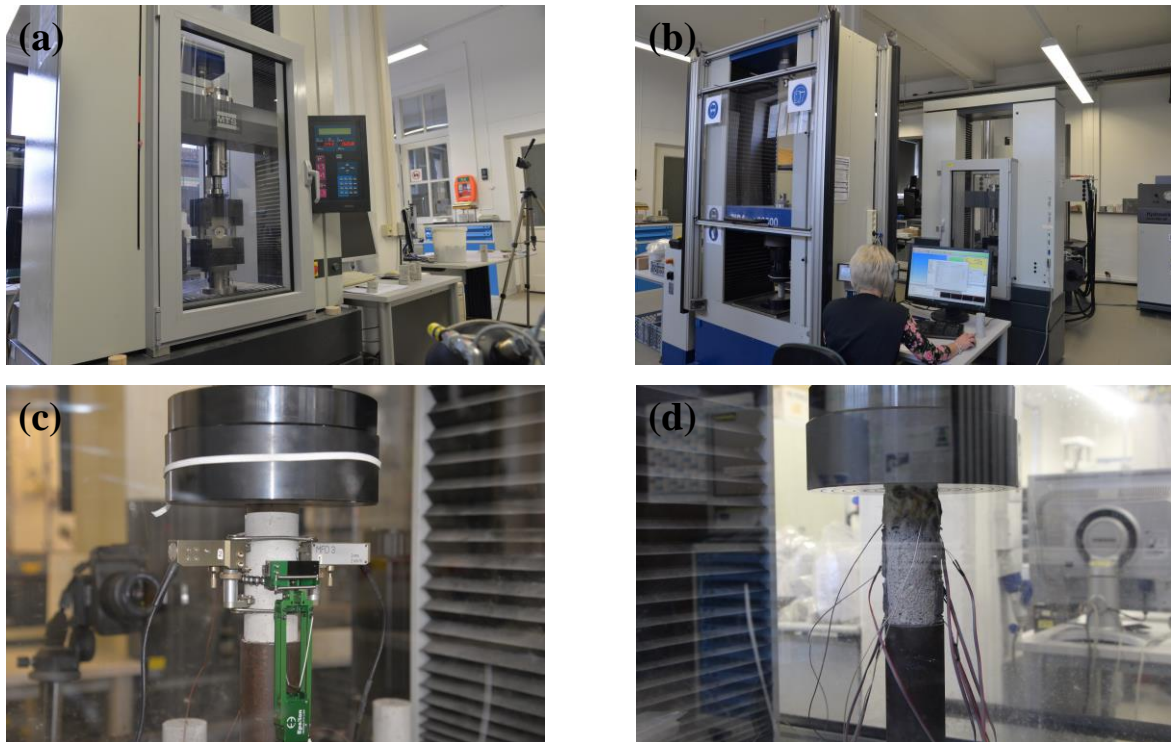


Fig. 3.3: (a) MTS 20/M (b) TIRA 28500 (c) LVDT and radial chain strain gauge (d) strain gauges to measure the strain at different parts of the specimen

Fig. 3.4a illustrates the setup of the ultrasonic wave senders and receivers. An AMSY-6 multi-channel AE measurement system with parallel measurement channels is used in this study. Small-scale piezoelectric AE sensors with full metal housing are attached directly to the specimen surface using thermoplastic glue. Due to their small size of approximately 5 mm diameter and their frequency response showing characteristic resonance at approximately 600 kHz, the sensors are well suited to trace local AE events at a laboratory scale. Utilizing the inverse piezoelectric effect, the AE sensors can be stimulated to act as ultrasonic senders by converting an electrical pulse into a mechanical pulse. Therefore, the same sensor array can be used alternately to monitor AE and to determine ultrasonic wave speed, respectively. A limitation of this bimodal use of the sensors is, of course, that the AE monitoring system cannot detect signals while acting as an ultrasonic sender in active mode. Therefore, some AE events might be missed and are not included in our evaluation. Fig. 3.4b illustrates the four AE sensors, which allow for parallel recording of AE events, such as AE counts and AE energy, at four parallel channels. The two groups of ultrasonic sensors are positioned at the top and middle part of the specimen, respectively, to independently measure the P-wave speed along the top and middle profiles.

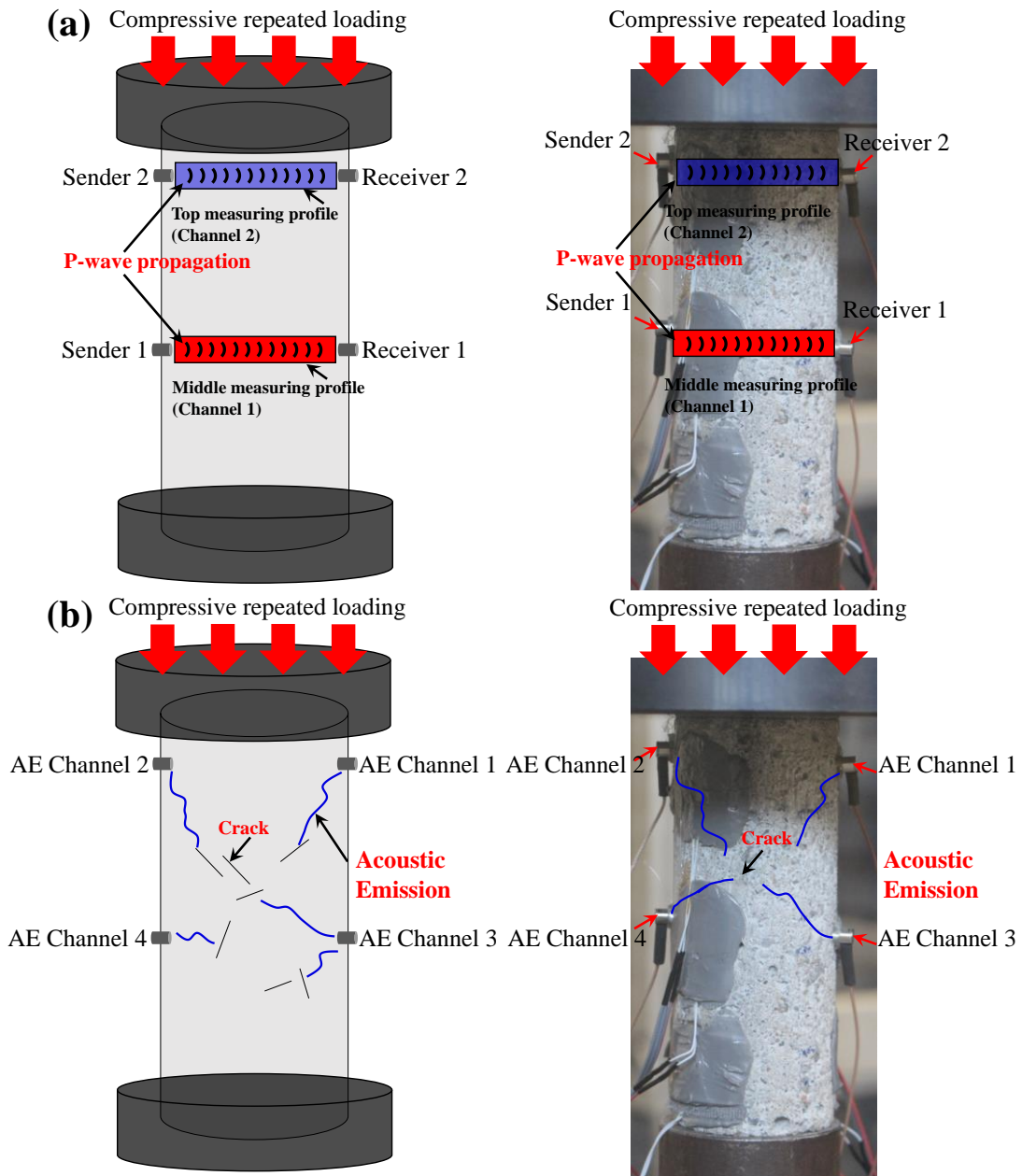


Fig. 3.4 Layout of (a) ultrasonic wave speed monitoring (b) AE monitoring system

Fatigue loading is applied as standard sinusoidal wave with constant peak-to-peak-amplitude during one loading stage. The fatigue loading schemes and the fatigue life (number of cycles up to failure) are listed in Table 3.2 and Table 3.3, respectively. According to the loading frequencies and the fatigue life, all the testing can be characterized as low frequency and low cyclic fatigue testing. The cyclic load level 40-80 means 40% UCS - 80% UCS, UCS for S1 = 18 MPa, UCS for S2 = 19 MPa. According to Table 3.2, the variations of both, maximum load stress σ_{max} and minimum load stress σ_{min} are considered.

Tab. 3.2: Fatigue testing scheme

Sample	Stage1	Stage2	Stage3	Stage4	Stage5	Stage6	Stage7	Stage8	Stage9	Stage10	Stage11
Cyclic load level normalized to %UCS											
S1-1	40-80	40-90									
S1-2	40-80	40-85	30-90								
S1-3	40-65	40-85	40-95								
S1-5	40-75	40-85	40-87.5	40-90	40-92.5						
S1-6	40-90										
S1-7	40-95										
S1-11*	40-90										
S1-12	40-90	40-95	40-97.5	40-100	40-102	40-105	40-107				
S1-8	50-90	40-90	30-90	25-90	20-90	15-90	10-90	10-95	10-97.5	10-100	
S1-10	30-90	20-90	10-90	10-95	10-97.5	10-100					
S2-13	40-60	40-65	40-70	40-75	40-80						
S2-14	40-75	35-75	30-75	25-75	20-75	15-75	10-75	5-75	5-80	5-85	5-90

* Sample unexpectedly broke during fatigue test and data is not available

Tab. 3.3: Number of cycles in each cyclic loading stage (St.)

Sam- ple	St. 1	St. 2	St. 3	St.4	St. 5	St. 6	St. 7	St. 8	St. 9	St. 10	St. 11	<i>f</i> [Hz]
Cycle number												
S1-1	50	3 F										0.4
S1-2	50	50	2 F									0.4
S1-3	2490	50	5 F									0.4
S1-5	2880	150	150	150	97 F							0.4
S1-6	34 F											0.4
S1-7	11 F											0.4
S1-11*	1 F											0.2
S1-12	500	150	150	150	150	150	53 F					0.8
S1-8	1250	150	150	150	150	150	150	150	150	52 F		0.4
S1-10	500	150	150	150	150	150	250 F					0.4
S2-13	150	150	150	150	11 F							0.5
S2-14	150	150	150	150	150	150	150	150	150	150	126 F	0.5

* Sample unexpectedly broke during fatigue test and data is not available; F: The sample failed in the current stage

3.2 Characteristics of dissipated energy

The continuum damage theory (CDT) and dissipated energy approach (DEA) are the two important approaches to investigate fatigue damage (Lei et al. 2017). Researchers adopted CDT to establish constitutive equations between the selected variables and damage evolution. A continuum damage model for fatigue load of concrete was established by Alliche (2004). This damage model can describe the material degradation under fatigue load by introducing tensorial damage parameters. Xiao et al. (2010) suggested that the damage variables should have a distinct physical meaning and should be measured and applied conveniently. The authors stated that axial residual strain is the most appropriate variable to reflect the damage evolution. Oneschkow (2016) investigated the evolution of strain and stiffness of high-strength concrete subjected to fatigue load. She found that the change of waveform from sinusoidal to triangular leads to larger values of strain and an increasing loss of stiffness. Baluch et al. (2003) established a damage model based on CDT for predicting the fatigue properties of concrete subjected to cyclic loading,

which is able to predict the residual strength of concrete subjected to initial damage induced by a given number of stress cycles. Lee et al. (2000) proposed a fatigue prediction model for asphalt concrete based on the elasto-visco-elastic correspondence principle. This model can account for the effects of loading rate and stress level on fatigue features. Generally, CDT can describe the evolution of damage based on constitutive equations. However, the damage variables selected in CDT always reflect single aspects, such as axial/radial strain or elastic modulus.

The DEA is able to reflect damage of materials during cyclic loading by considering the energy dissipated or absorbed by the sample. Compared to CDT, DEA has the following advantages:

- DEA can consider strain and stress concurrently and is more precise compared to the CDT which only considers a single damage variable
- During the stationary stage of fatigue test, the increment of strain is hard to measure to characterize the damage due to the extremely small change of strain. The DEA can still clearly reflect the dissipated energy in the stationary stage, and continuously represent the progressive damage.

Bagde & Petroš (2009) found that the dissipated energy is increasing with frequency and load amplitude. The energy dissipated by the rock could be treated as an inherent characteristic. Lei et al. (2017) proposed a concrete fatigue life prediction method, which is based on accumulated dissipated energy. It was concluded that the dissipated energy within each cycle has a direct relationship with stress levels. Tepfers et al. (1984) investigated the energy absorption of plain concrete in fatigue tests and found that the absorbed energy at failure under uniaxial compression seems to be the same for static load as well as for fatigue load. Xie et al. (2004, 2005) discussed the intrinsic relations between dissipated energy, energy release, and structural failure of rocks during loading and unloading stages and stated that dissipated energy acts as an internal factor connected with damage and irreversible deformation. Naderi & Khonsari (2013) performed a series of fatigue tests on glass/epoxy laminates. He concluded that when the load is relatively low, the dissipated energy due to damage is small compared to dissipated energy due to heat. With increasing load level, the proportion of dissipated energy due to damage increases. Jiang et al. (1994) and Tong et al. (1989) suggested that the accumulated dissipated energy can be used as a proper variable to reflect the damage of materials because there is no discontinuity in the curve. Shadman & Ziari (2017) proposed an approach based on dissipated energy to predict fatigue life of porous asphalt. The authors found that the total dissipated energy at failure can be forecasted by regression equations relating cycle number and total dissipated energy. Shen et al. (2006) pointed out that the fluctuation of energy dissipation between two consecutive cycles can indicate the development of damage.

Many researchers found that maximum load level during cyclic loading has an influence on fatigue of the material. Ge et al. (2003) investigated the threshold value (endurance limit) of load level during fatigue tests. He mentioned that in case the maximum load level is smaller than the threshold value, the axial, radial and volumetric irreversible strain tend to be constant. However, when maximum load level is larger than the threshold value, axial, radial and volumetric irreversible strain increase with increasing number of load cycles. Rao & Ramana (1992) conducted fatigue tests on Hyderabad granites. They concluded that when load level is larger than threshold value, the Kaiser Effect and AE events are more pronounced and that the threshold value is comparable to the dilatancy limit. Concrete as quasi-brittle material is always exchanging (absorbing and releasing) energy with its surrounding system during cyclic loading (Dattoma & Giancane 2013; Lei

et al. 2017; He et al. 2018). The amount of dissipated energy during one single cycle reflects the ability of the material to resist damage induced by external loading. The more energy during one cycle is dissipated the more damage is generated inside the material. The total dissipated energy of a sample can be generally divided into two parts:

- dissipated by heat convection, conduction and radiation of seismic energy
- defect formation, crack propagation and plastic deformation.

The dissipated energy by heat convection and conduction remains almost constant during cyclic loading (Dattoma & Giancane 2013), therefore the change in dissipated energy is directly related to fatigue evolution.

This chapter is based on DEA to investigate the characteristics of dissipated energy of concrete samples subjected to stress-controlled uniaxial cyclic loading. The effect of cyclic load levels on characteristics of dissipated energy is quantitatively investigated. The dissipated energy within the DEA concept is compared with variables used in CDT and the evolution of damage variables in the two approaches is analysed.

The dissipated energy density U_d within one single cycle is defined as the area of the hysteresis loop in the stress (σ) - axial strain (ε_a) - diagram (Tepfers et al. 1984; Lei et al. 2017; He et al. 2018; Song et al. 2018). The unit of U_d is J/m^3 and it represents the dissipated energy in a unit volume. The accumulated dissipated energy density U_a is the sum of single cycles U_d from the beginning of cyclic loading until the current cycle N . The axial strain ε_a is measured through axial strain gauge placed at the central part of the sample. U_d and U_a are defined by Equation 3.1 and Equation 3.2.

$$U_d = \oint \sigma d\varepsilon_a \quad (3.1)$$

$$U_a = \sum_{i=1}^N U_d \quad (3.2)$$

3.2.1 Effect of maximum cyclic load level on energy dissipation

U_d for different maximum cyclic load levels is plotted in Fig. 3.5. Among the six samples (S1-1, S1-2, S1-3, S1-5, S1-6 and S1-7), only S1-6 and S1-7 experienced cyclic loading at one stage only until failure (40% - 90% UCS and 40% - 95% UCS, respectively). The first 50 cycles at different load levels were used to analyse U_d . Like shown in Fig. 3.5, the curves for U_d of S1-6 and S1-7 are "U"-shaped. The fatigue life of S1-6 and S1-7 are 34 and 11 cycles, respectively. U_d of S1-6 and S1-7 is almost symmetrical along the middle point of fatigue life (17th cycle and 5th cycle). The minimum value of U_d is also observed at the 17th and 5th cycle, respectively. Considering these characteristics, the minimum value of U_d can be used to predict the fatigue life of materials under cyclic loading with only one loading stage.

According to table 3.2, S1-1 and S1-2 experienced cyclic loading between 40% - 80% UCS in the first stage (without any former cyclic loading stages). U_d of S1-1 and S1-2 is plotted in Fig. 3.6a. The values of U_d are highly coincident, which demonstrates the same material has similar characteristics of energy dissipation under the same loading strategy. In addition, from Fig. 3.6a to Fig. 3.6d, it can be observed that U_d is sensitive to the change of cyclic load level and can be selected as an inherent damage variable.

According to Table 3.2, S1-2, S1-3 and S1-5 experienced loading between 40% - 85% UCS with different cyclic loading stages before. In detail, the S1-2, S1-3 and S1-5 experienced 40% - 80% UCS, 40% - 65% UCS, and 40% - 75% UCS in first stage before

cyclic loading between 40% - 85% UCS was applied. U_d of S1-2, S1-3 and S1-5 are plotted in Fig. 3.6b. In terms of U_d it holds: $S1-2 > S1-3 > S1-5$. Rao and Ramana (1992) stated that the threshold value for fatigue is comparable to the dilatancy limit. This limit usually corresponds to about 80% UCS (Ge & Lu 1992; He et al. 2014). Consequently, the first cyclic loading stage for S1-2 (40% - 80% UCS) can already result in massive fatigue damage inside the sample. Therefore, compared to S1-3 and S1-5, S1-2 is more damaged. In addition, from the first to the second cyclic loading stage, the increments of load amplitude for S1-3 and S1-5 are 20% UCS and 10% UCS, respectively. Therefore, U_d of S1-3 is significantly larger than that of S1-5.

Different from S1-1 and S1-2, S1-5 and S1-6 experienced the same cyclic load level but applied in different loading strategies (see Table 3.2). S1-5 experienced cyclic loading between 40% - 90% UCS after three former cyclic loading stages (40% - 75% UCS, 40% - 85% UCS, and 40% - 87.5% UCS). S1-6 experienced only a single cyclic loading stage between 40% - 90% UCS until failure. U_d is represented in Fig. 3.6c. S1-5 did not fail after 50 cycles whereas S1-6 broke after only 34 cycles at same cyclic load level. Fig. 3.6c documents that U_d of S1-6 is significantly larger than that of S1-5. U_d of S1-6 reveals a "U" shape. This demonstrates, that samples can have a different amount of dissipated energy in the same cyclic load level. The loading strategy can influence the amount of dissipated energy. Progressively increasing maximum load, for example the maximum load level of S1-5 increased from 75% UCS to 90% UCS, will lead to less dissipated energy compared to cyclic loading at only one stage, for example for S1-6. This phenomenon may be explained by energy transmission and crack propagation. The moderate increasing of load level in cyclic loading, such as for sample S1-5, can result in more evenly distributed micro cracks and more even transmission of energy. This can avoid the rupture of sample in extremely short time due to initial large load level. According to Table 3.2, S1-5 experienced 5 cyclic loading stages. U_d for S1-5 is illustrated in Fig. 3.6d. With increasing maximum load level from 75% UCS to 92.5% UCS, the evolution of U_d changes. As shown in Fig. 3.6d, it becomes obvious that U_d increases with increasing of load level from 40% - 75% UCS to 40% - 92.5% UCS.

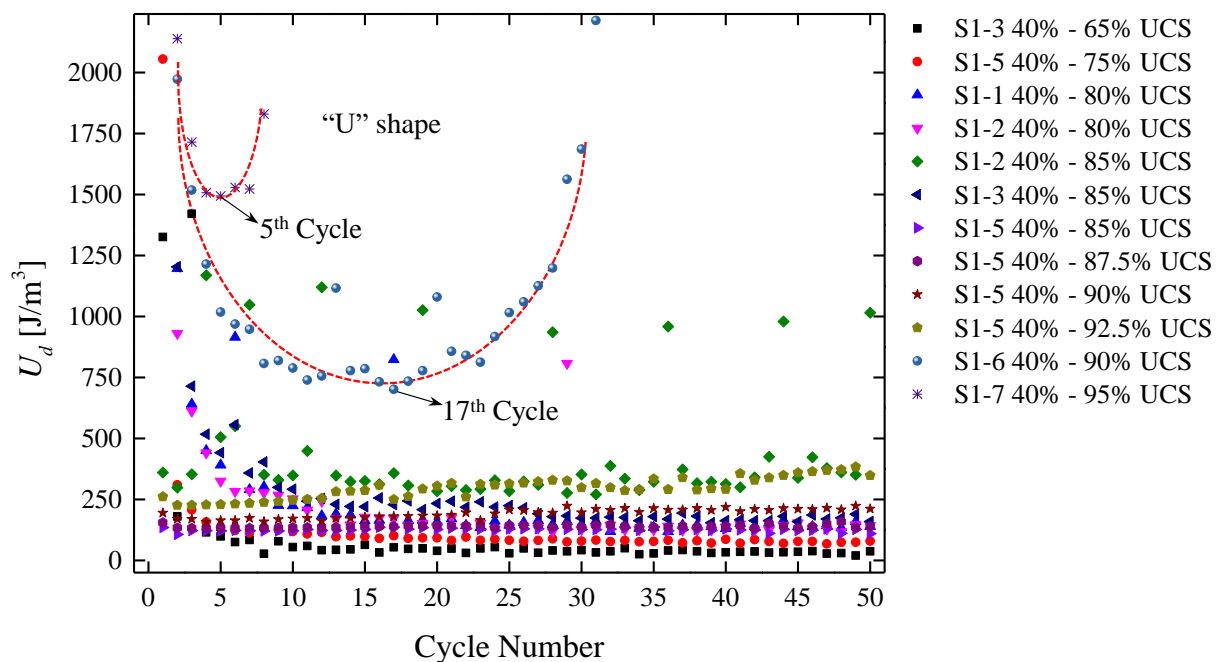


Fig. 3.5: U_d for different maximum cyclic load levels

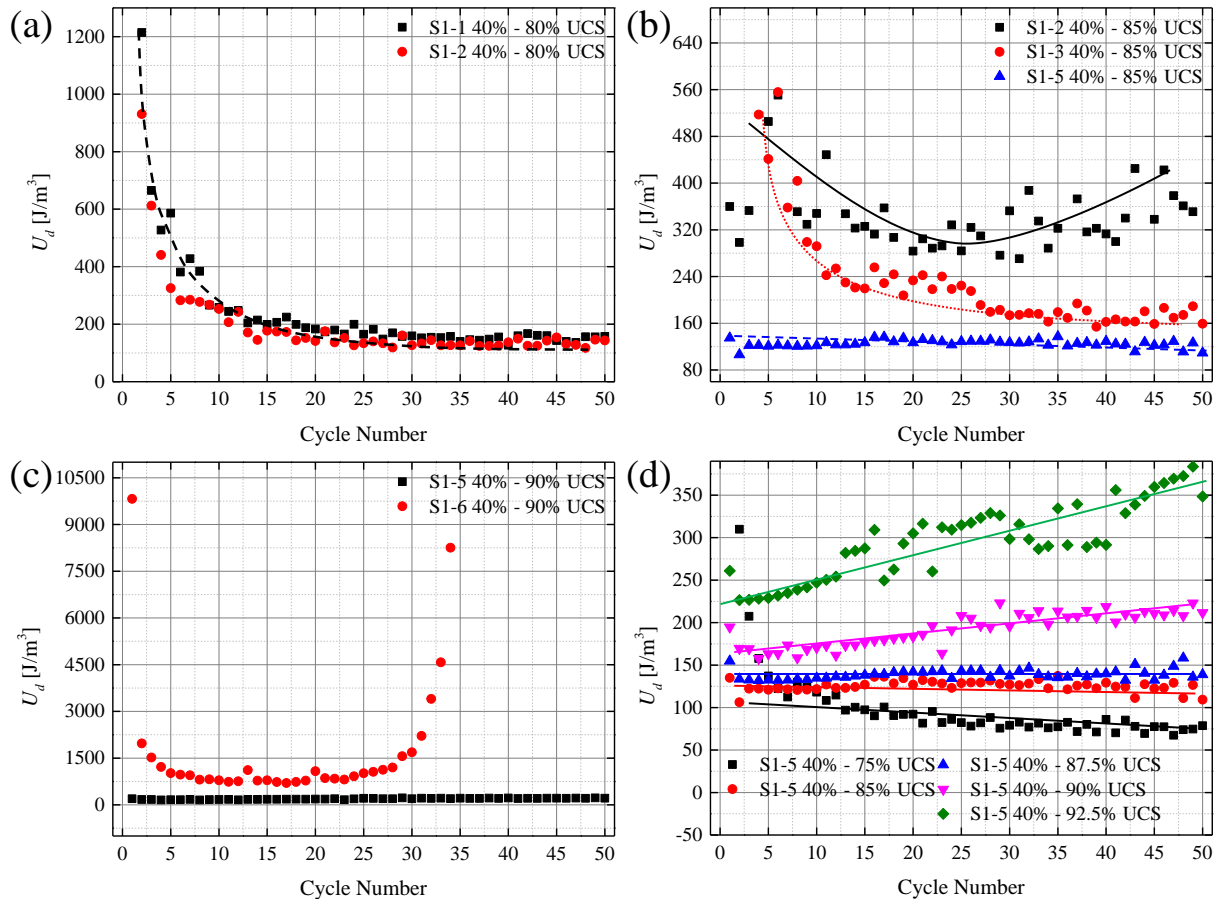


Fig. 3.6: (a) U_d between 40% and 80% UCS (b) U_d between 40% and 85% UCS (c) U_d between 40% and 90% UCS (d) U_d of S1-5 (5 cyclic loading stages)

U_a registered in different cyclic load levels is illustrated in Fig. 3.7. S1-6 and S1-7 broke within one single cyclic load level. U_a of S1-6 and S1-7 are “inverted-S” shaped and can be divided into three phases:

- decelerating phase
- stationary phase
- accelerating phase - similar to the evolution of residual axial strain in fatigue tests (Xiao et al. 2009) and also common in classical creep tests.

The cycle number in phase 1 is almost equal to the cycle number in phase 3. The slope of the curve of S1-7 is larger than that of S1-6 for the same number of cycles. Apart from S1-6 and S1-7, all other samples show only the first or the second phase during the first 50 cycles.

U_a of S1-1 and S1-2 is illustrated in Fig. 3.8a. The slope of U_a during the stationary phase reflects the speed of energy dissipation. The load level in the first cyclic stage of S1-1 and S1-2 are both 40% - 80% UCS. According to Fig. 3.8a, the slope of U_a during the first 10 cycles show some scatter, which is caused by small differences in the physical properties of the samples. However, the slope for U_a of S1-1 and S1-2 are nearly identical (see values of β_1 , β_2) for same cycle number during the stationary phase, hereon the stationary phase is designated as the phase in which the slope of U_a curve remains constant, as plotted in Fig. 3.8a. S1-1 and S1-2 entered the stationary phase after nearly the same number of cycles (around 12 cycles). This demonstrates that the speed of energy

dissipation in the stationary phase is constant for a certain cyclic loading strategy and can therefore be selected as variable to represent fatigue damage of materials.

U_a of S1-2, S1-3 and S1-5 in 40% - 85% UCS cyclic load level is illustrated in Fig. 3.8b. As shown in Fig. 3.8b, S1-2 and S1-5 do not have a decelerating phase but only the stationary phase. However, S1-3 shows both, the decelerating and stationary phase. As can be seen from Fig. 3.7 and Fig. 3.8a, the curves of U_a during the first cyclic loading stage show at least the first two or all three phases, like for S1-6 and S1-7. Curves of U_a after the first cyclic loading stage usually only show the stationary phase. This phenomenon can also be observed in Fig. 3.8c and Fig. 3.8d. As Fig. 3.8b documents, S1-2 has the largest slope (see β_1) due to massive damage resulting from former cyclic loading stage (40% - 80% UCS) in which the maximum load level is close to the fatigue threshold value. Due to the damage in former cyclic loading stage, the ability of S1-2 to resist external load decreases and consequently the speed of energy dissipation is larger than that of S1-3 and S1-5. The load increments for S1-3 and S1-5 are 20% UCS (from 65% to 85%) and 10% UCS (from 75% to 85%), respectively. Larger increments can result in larger slope values for U_a (see Fig. 3.8b).

U_a of S1-5 and S1-6 in the 40% - 90% UCS cyclic load level is illustrated in Fig. 3.8c. The slope of U_a curve for S1-6 in the stationary phase is consistently larger than that of S1-5. S1-6 experienced only one cyclic load level (40% - 90% UCS) up to failure and the curve shows all three phases. However, due to former cyclic loading stages, S1-5 shows only the stationary phase. This indicates that the former cyclic loading stages with small load level lead to less energy dissipation compared to samples that only experience one single cyclic load level. The reason might be that the former cyclic loading stages with small load level progressively consolidated the sample which improves the ability to resist external load. U_a of S1-5 for five consecutive cyclic loading stages are illustrated in Fig. 3.8d. As shown in Fig. 3.8d, only the first cyclic loading stage (40% - 75% UCS) shows the decelerating phase, the latter four stages only show the stationary phase. By progressively increasing the maximum load, the slope of U_a increases. This confirms that during cyclic loading the maximum load directly influences the release of dissipated energy (Tepfers et al. 1984; Lei et al. 2017).

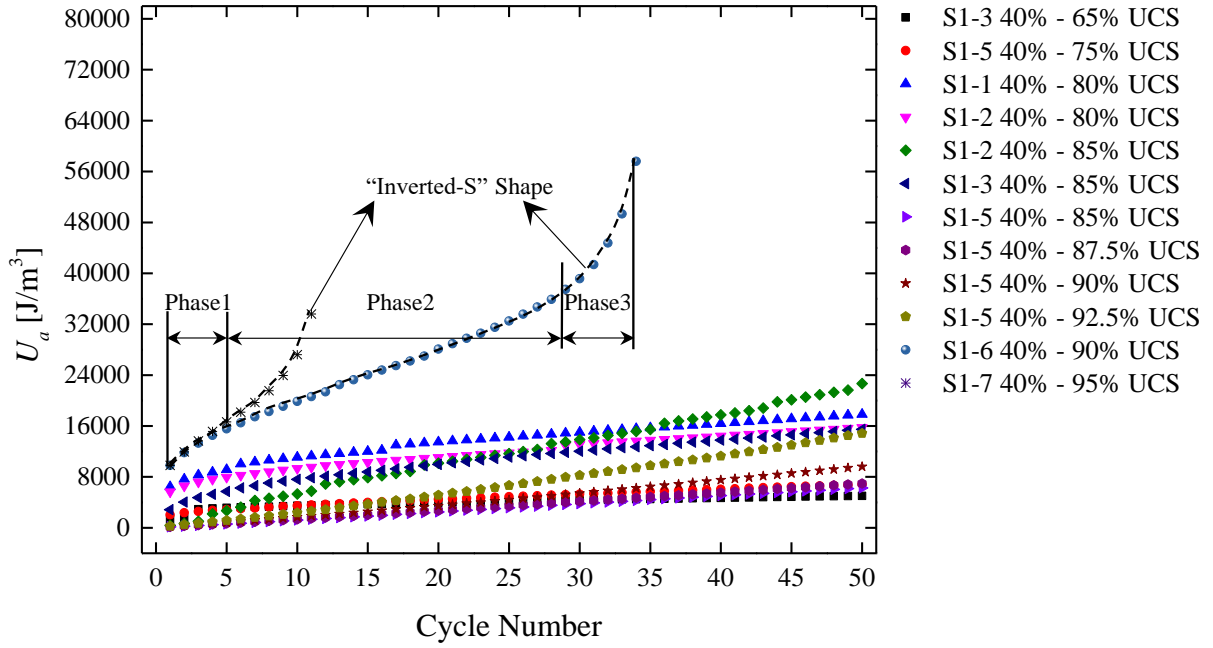


Fig. 3.7: U_a for different maximum cyclic load levels

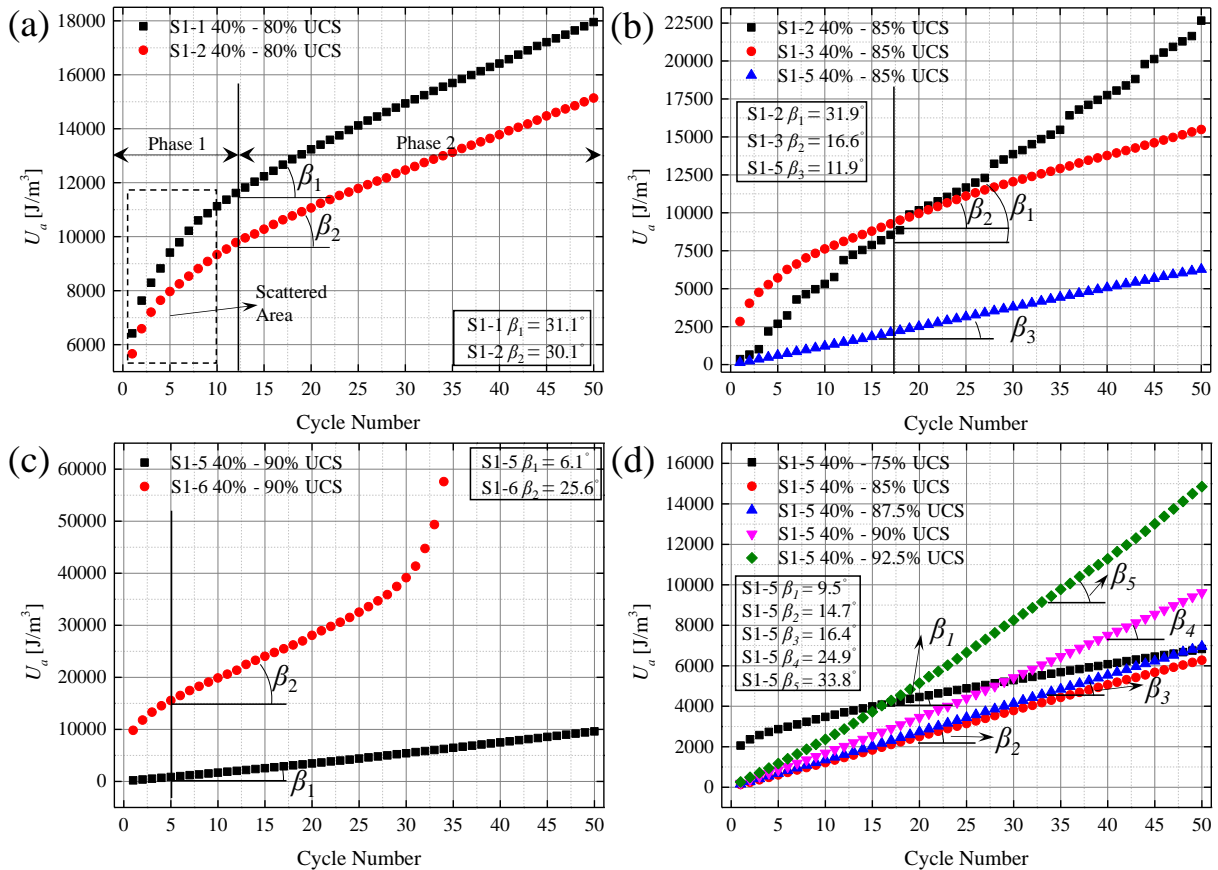


Fig. 3.8: (a) U_a between 40% and 80% UCS (b) U_a between 40% and 85% UCS (c) U_a between 40% and 90% UCS (d) U_a of S1-5 (5 cyclic loading stages)

3.2.2 Effect of minimum cyclic load level on energy dissipation

U_d for different minimum cyclic load levels is plotted in Fig. 3.9a. The first 100 cycles in the different cyclic load levels are used to analyse U_d . It should be noted that the samples did not break during loading process listed in Table 3.2, therefore the maximum load level is enhanced to obtain sample failure. 30% - 90% UCS is used for the first cyclic loading stage for S1-10. S1-8 has experienced four preceding cyclic loading stages until a load level at 30% - 90% UCS is reached. After cyclic loading at 30% - 90% UCS, both samples experienced the same cyclic loading at 20% - 90% UCS and later at 10% - 90%. As shown in Fig. 3.9a, S1-10 shows smaller values of U_d than S1-8 in the same stage. During cyclic loading at 20% - 90% UCS and 10% - 90% UCS, the difference of U_d is obviously. This also verifies: when maximum load is larger than threshold value of fatigue (80% UCS), massive damage is induced. Therefore, the damage of S1-8 (four former loading stages with maximum load larger than 90% UCS) will be more serious than S1-10. U_d for different minimum cyclic load levels of S1-8 are plotted in Fig. 3.9b. U_d increases with decreasing values of minimum cyclic load level. The decrease of minimum cyclic load level in the first four cyclic loading stages is 5% UCS and later one 10% UCS. Fig. 3.9b indicates a non-linear increase in energy release with decreasing minimum cyclic load level.

U_a for different minimum cyclic load levels is plotted in Fig. 3.10a. The two later cyclic loading stages (20% UCS - 90% UCS and 10% UCS - 90% UCS) show obviously different slopes for S1-8 and S1-10 which represents different speed of damage evolution. According to loading strategies shown in Table 3.2, this indicates again: due to the fact that S1-8 experienced four former loading stages and the maximum load levels in all four former stages are larger than threshold value of fatigue damage (80% UCS), the speed of damage evolution for S1-8 is larger than that of S1-10 in 20% UCS - 90% UCS and 10% UCS - 90% UCS stages. U_a for sample S1-8 at different minimum cyclic load levels and fixed maximum load level of 90% UCS is plotted in Fig. 3.10b. A clear trend becomes obvious: the cumulative speed of dissipated energy increases if span between maximum and minimum load level increases. This also verifies the effect of minimum cyclic load level on cumulative dissipated energy. It shows that both maximum and minimum load have obvious effect on amount of dissipated energy.

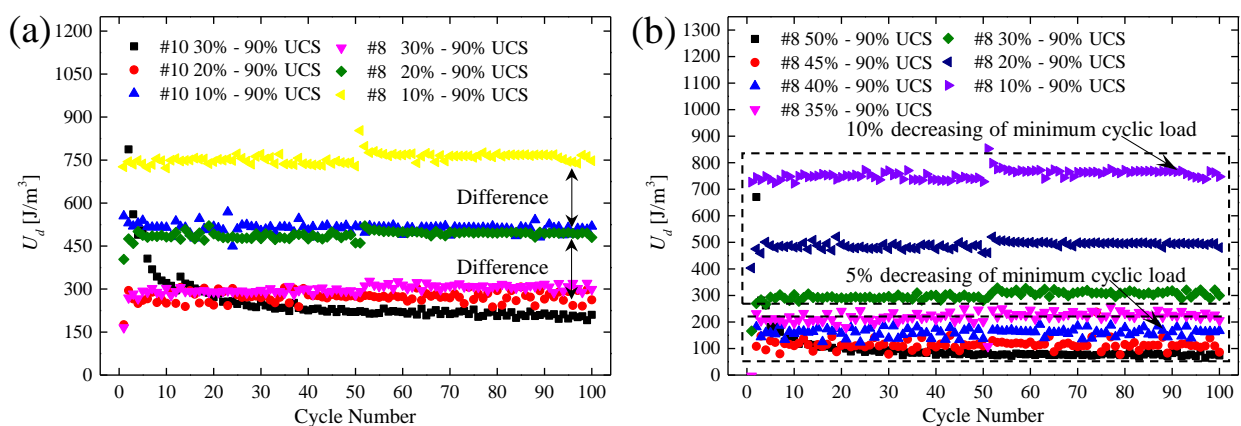


Fig. 3.9: (a) U_d of S1-8, S1-10 (b) U_d of S1-8 versus cycle number for different minimum cyclic load levels

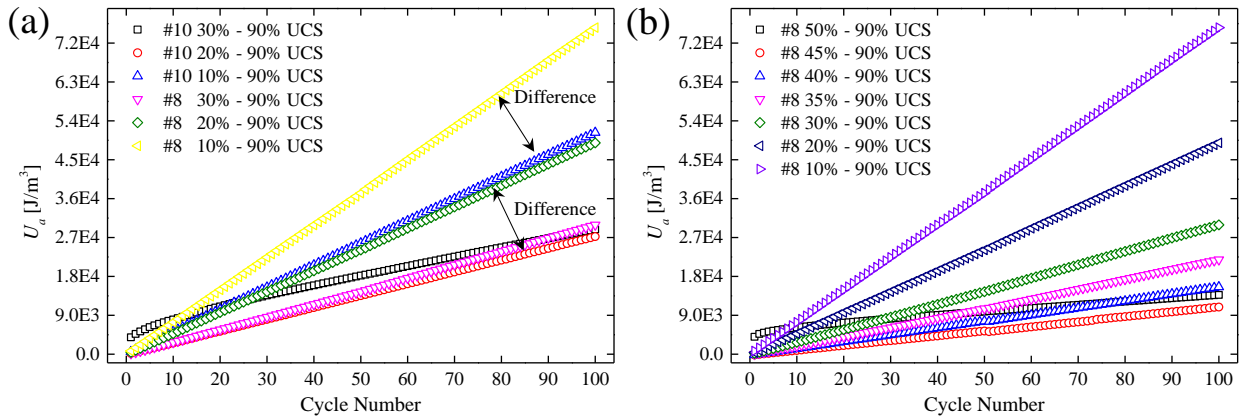


Fig. 3.10: (a) U_a of S1-8, S1-10 (b) U_a of S1-8 versus cycle number for different minimum cyclic load levels

3.3 P-wave speed evolution and AE characteristics

The monitoring of P-wave speed is a practical approach to characterize the damage of a sample during an experiment. In order to draw general conclusions of P-wave speed evolution during fatigue loading, four cyclically-loaded samples of Series 1 and Series 2 (S2-13, S2-14, S1-10, S1-8) are selected for detailed analysis, see Fig. 3.11. The measurements of P-wave speed are conducted along two different profiles, which represent the damage evolution at the top and middle part of the concrete samples, see Fig. 3.4. Sample S2-13 undergoes the following loading strategy: σ_{min} is fixed to 40% UCS and σ_{max} is gradually increased from 60% UCS to 80% UCS. However, samples S2-14, S1-10 and S1-8 experience a different loading strategy: first σ_{max} is fixed and σ_{min} is reduced, then σ_{min} is fixed and σ_{max} is gradually increased.

It can be observed from Fig. 3.11a that the evolution of P-wave speed for sample S2-13 shows three distinct phases, whereas the other three samples show four phases (Fig. 3.11b – Fig. 3.11d). This is due to the fact that sample S2-13 does not experience the loading stage where σ_{min} decreases and σ_{max} is fixed. In respect to the P-wave-speed the four stages are characterized by:

- Initial strong drop
- Constant phase
- Decreasing phase
- Sharp decline and failure

The four-stage feature is visible for formerly tested samples S1-8 and S1-10 as well as S2-14. The effect of σ_{min} on the P-wave speed evolution can be deduced from the second stage. It is obvious that the P-wave speed for both profiles remains almost constant even when σ_{min} reduces by a large amount (for S1-8: from 50% to 10% UCS and for S2-14 from 40% to 5% UCS), whereas σ_{max} is fixed. This indicates that σ_{min} has very limited (insignificant) impact on P-wave speed evolution during cyclic loading. The missing of the second stage for sample S2-13 also indirectly confirms this observation. By increasing σ_{max} of S1-8, S1-10 and S2-14 the third stage with its typical decrease of P-wave speed is started. Considering both measuring profiles, all the four samples experience a more noticeable damage at the top part during the first stage. This can be attributed to the stiffness effect of loading platen and direct, dynamic loading by the moving upper loading platen. The stiffness contrast between the platen and top part of the sample will result in local crack propagation. When the samples are close to failure - typically at the end of the

third stage or at the begin of the fourth stage, the P-wave speed in the middle part decreases more pronounced than in the top part and the P-wave speed of the two profiles reach an approximately identical value which is defined as “equal point” in Fig. 3.11. The equal point as shown in Fig. 3.11 is a precursor to predict the fatigue failure of concrete.

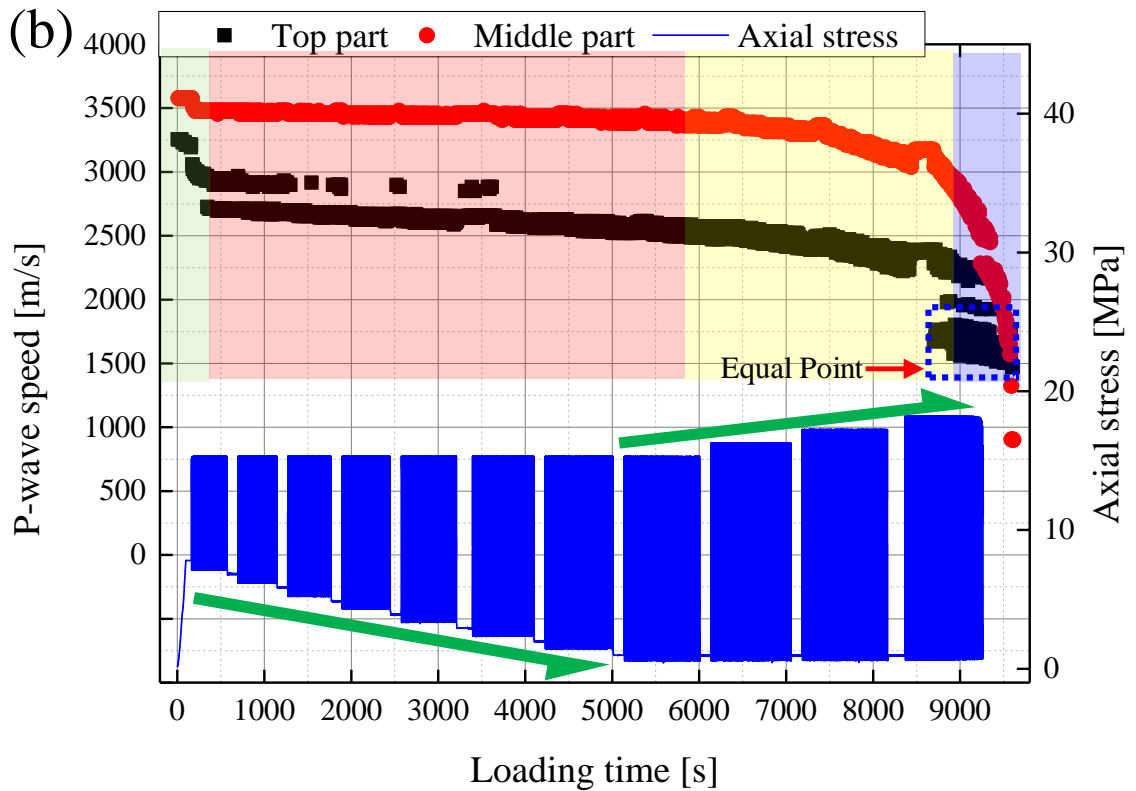
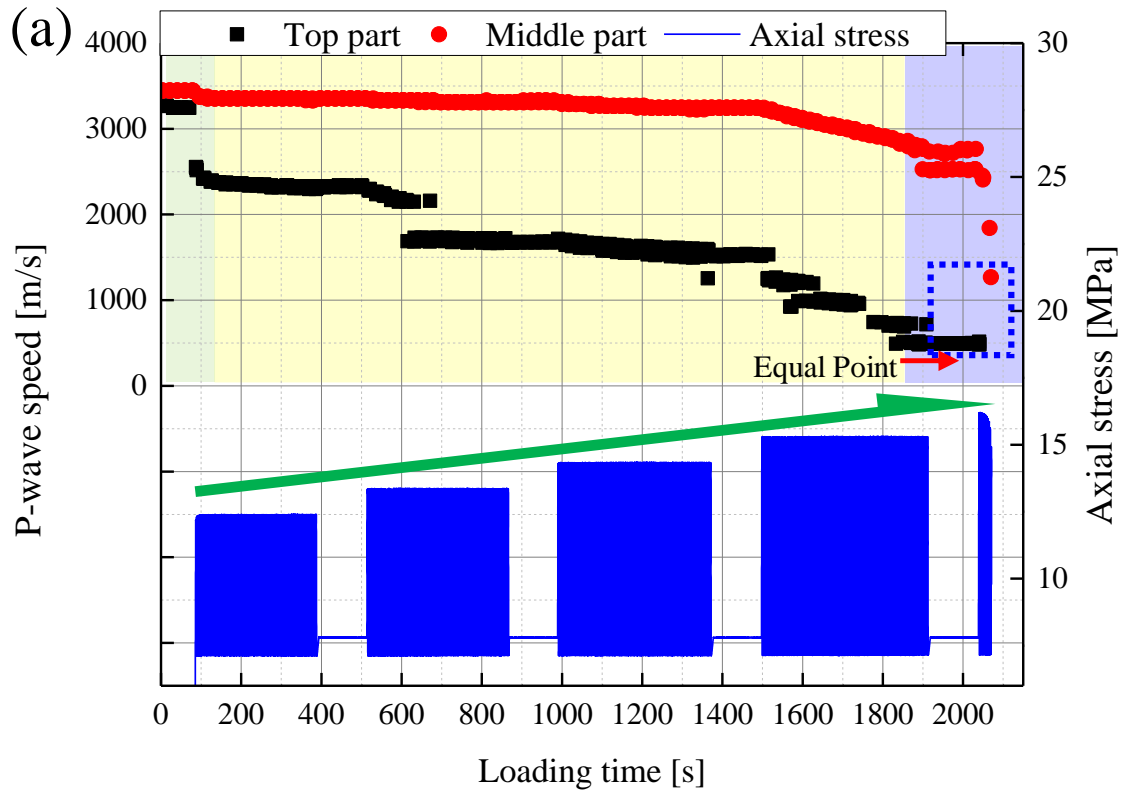
To characterize the evolution of the P-wave speed along the two profiles, a P-wave ratio is defined as: V_m/V_t , where V_m is the P-wave speed measured at the middle part of the sample and V_t is the P-wave speed measured at the top part of the sample. The evolution of P-wave ratio for samples S2-13, S2-14, S1-10 and S1-8 is illustrated in Fig. 3.12. The P-wave ratio of the four concrete samples reveal three stages:

- Slow increase
- Obvious increase reaching peak point at the end
- Sharp decline and failure

The P-wave ratio is small (usually only slightly larger than 1) in the first stage. This is induced by the more pronounced reduction of the P-wave speed in the top part of the sample. During this stage, the top profile shows a slightly larger P-wave speed reduction than the middle profile and this leads to the slight increase of the P-wave ratio. The first stage covers both two kinds of loading strategies:

- fixed σ_{max} and gradual reduction of σ_{min}
- fixed σ_{min} and gradual increase of σ_{max} .

The second stage includes the peak value of the P-wave ratio. The P-wave speed reduction rate of the two profiles are equal at the peak point. After the peak point, the reducing speed of the middle part is larger than that of the top part leading to a decrease of P-wave ratio. Failure of the sample usually happens shortly after the peak point. The value of the P-wave ratio at failure is close to 0.3 (the value for sample S2-13 is larger, maybe induced by applying loading strategy number one). Compared with the P-wave speed, the P-wave ratio is more general applicable. The peak point as shown in Fig. 3.12 is more convenient to be used as failure precursor than the equal point in Fig. 3.11.



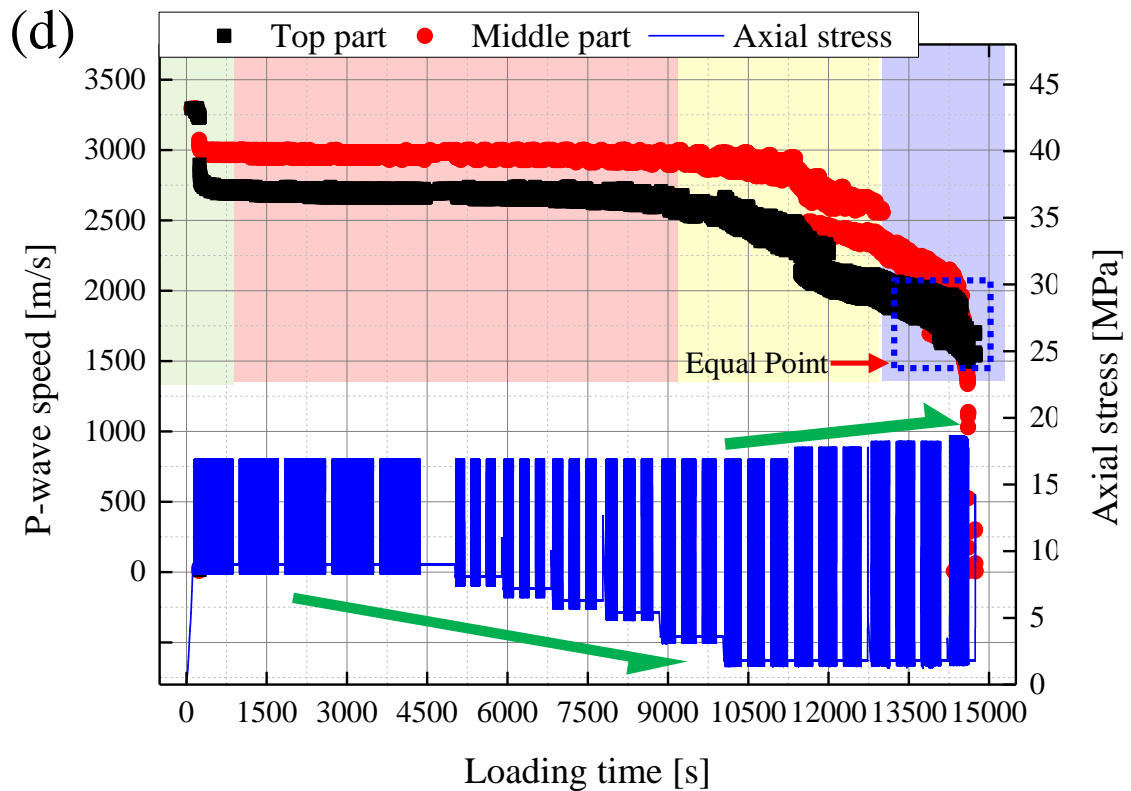
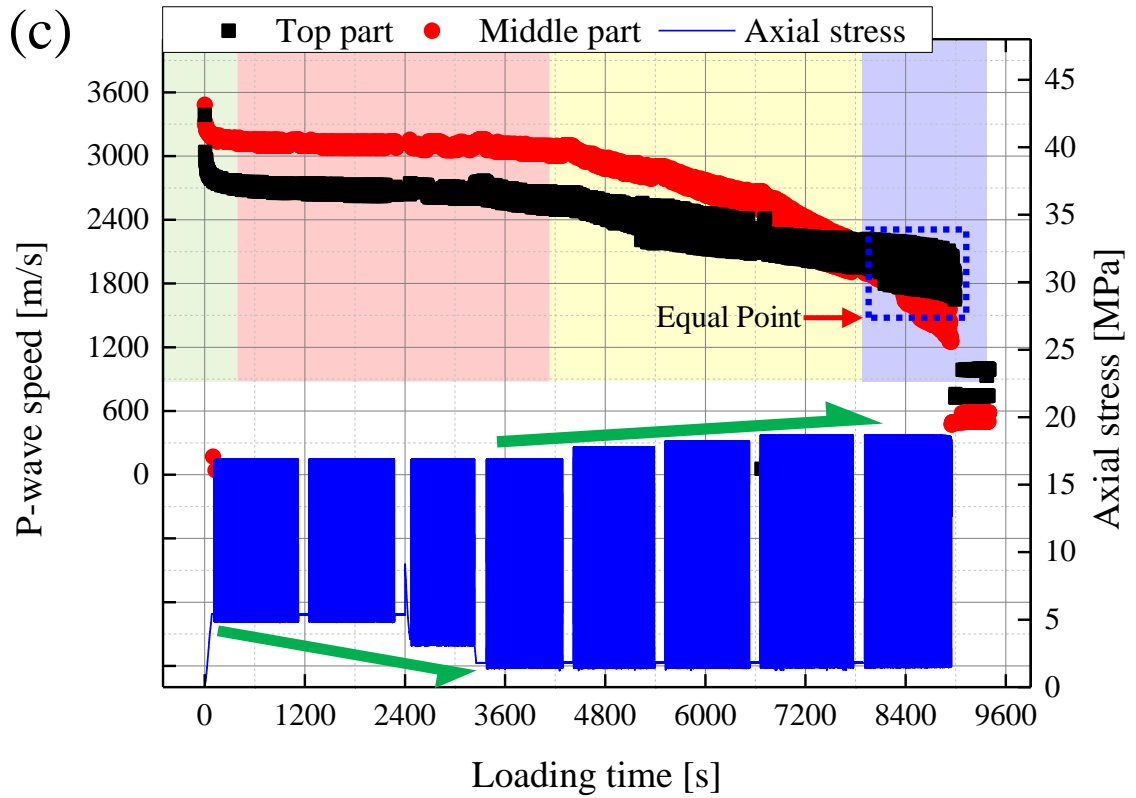
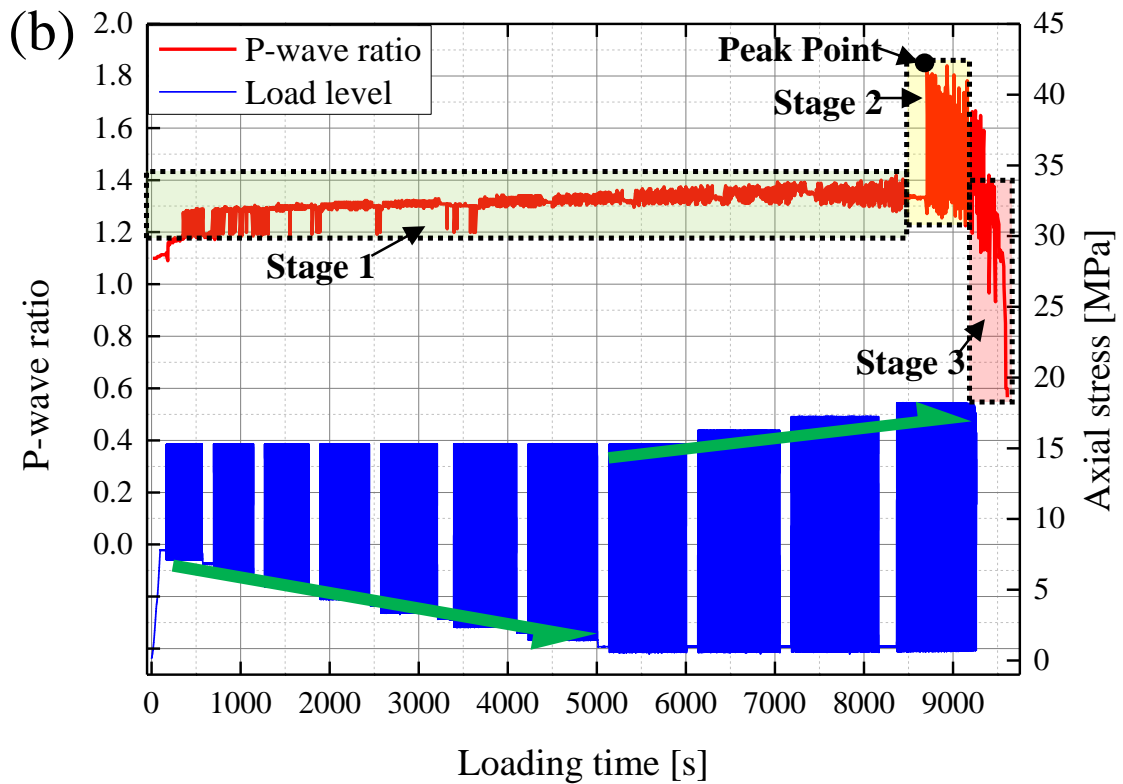
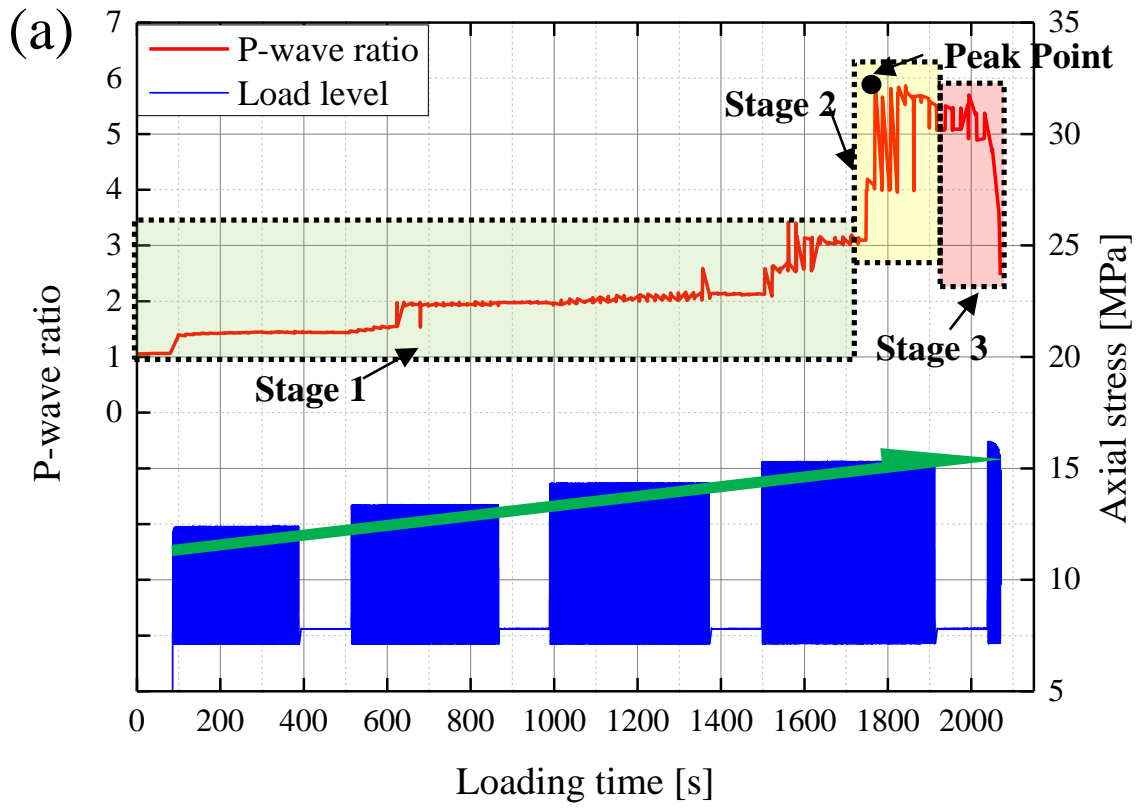


Fig. 3.11: P-wave speed evolution for (a) S2-13 (b) S2-14 (c) S1-10 (d) S1-8



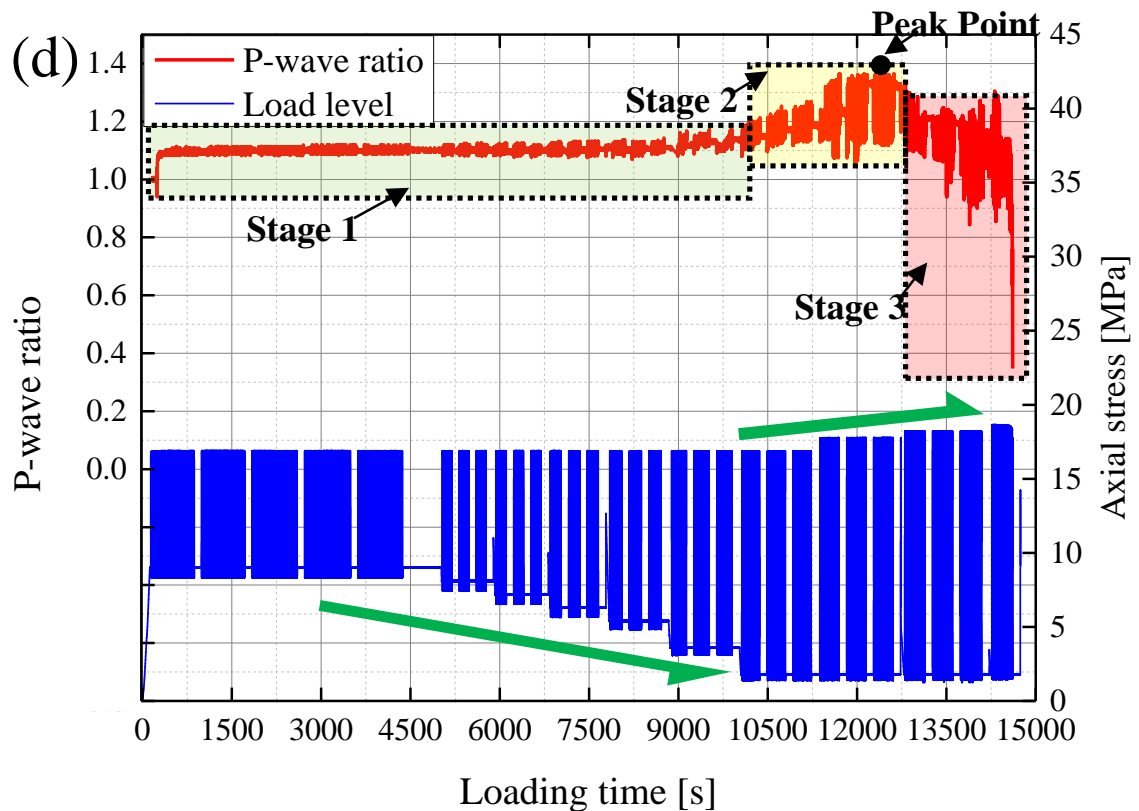
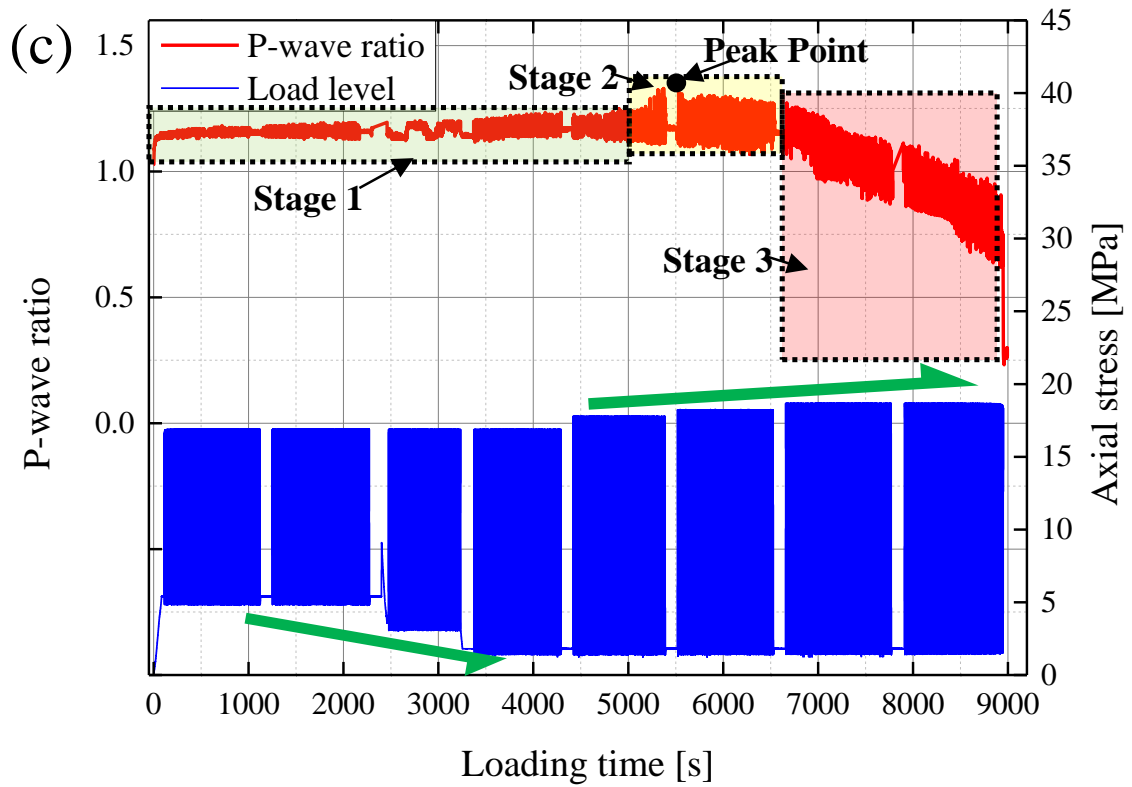
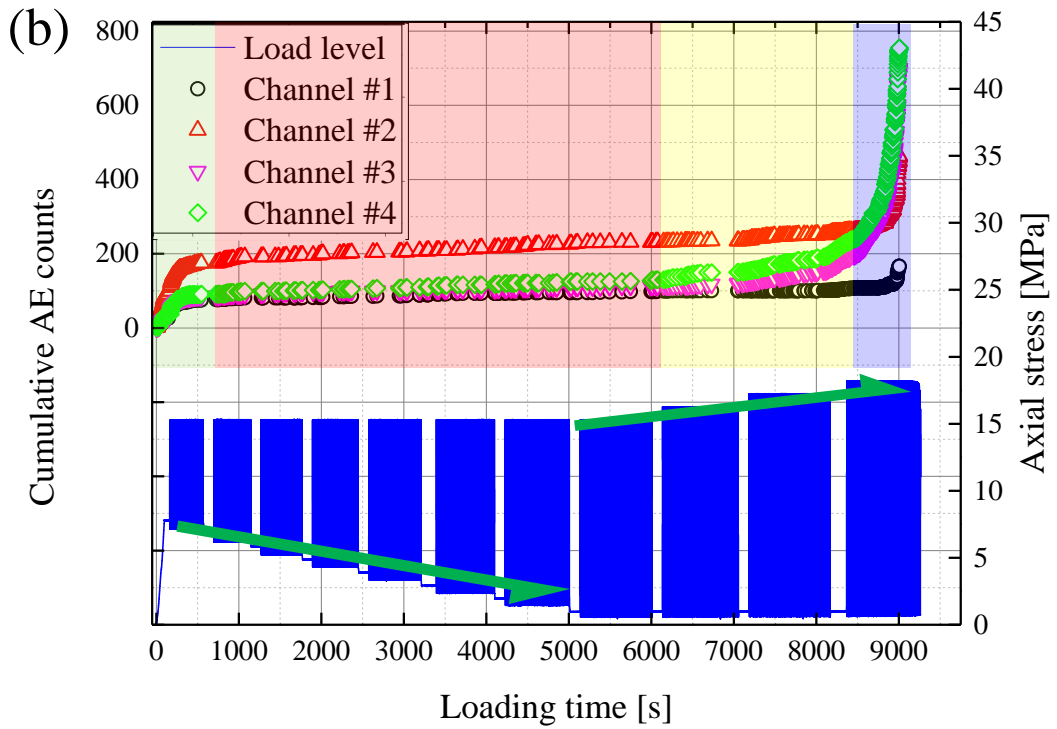
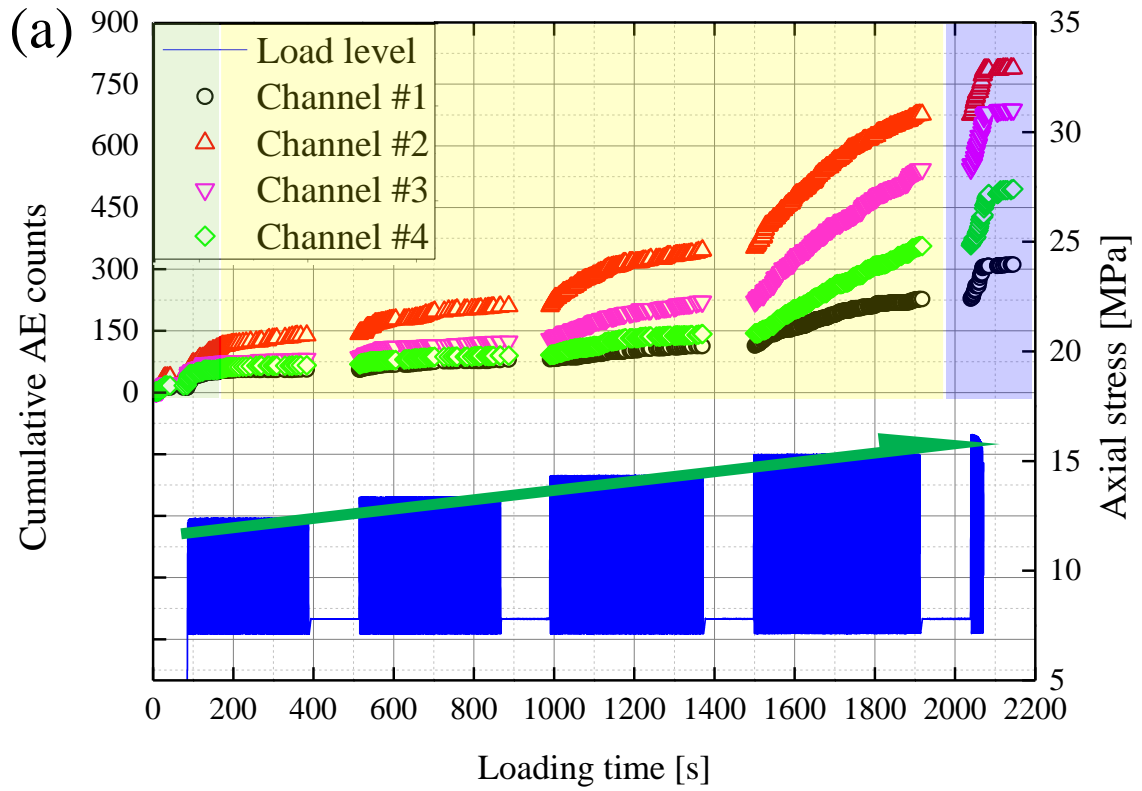


Fig. 3.12: P-wave ratio evolution for (a) S2-13 (b) S2-14 (c) S1-10 (d) S1-8

The AE events are analysed in terms of cumulative AE counts and AE energy. Fig. 3.13 and Fig 3.14 illustrate that the four-stage characteristic also fits to describe the evolution of cumulative AE counts and energy when the samples experienced two loading strategies:

- Short initial phase with strong non-linear increase in AE activity
- Phase with moderate, nearly linear increase in AE activity
- Phase of significant accelerating of AE activity
- Failure

The effect of σ_{min} on AE counts and energy is also minimal, similar to the effect on P-wave speed. Due to the fact that sample S2-13 has experienced only one loading strategy (σ_{min} is fixed and σ_{max} is gradually increased), the rate of AE counts and energy is gradually rising and stage 2 is missing. The increasing rate in stage 3 for sample S2-13 is larger than for the other three samples, which indicates that the decrease of σ_{min} in former loading stages may be beneficial to reduce the increasing rate of AE counts and energy. This can also be interpreted as follows: stage 2 is acting as a “cushion” role before stage 3, so the increasing rate in stage 3 is smaller compared with the stage 3 without experiencing stage 2 before.



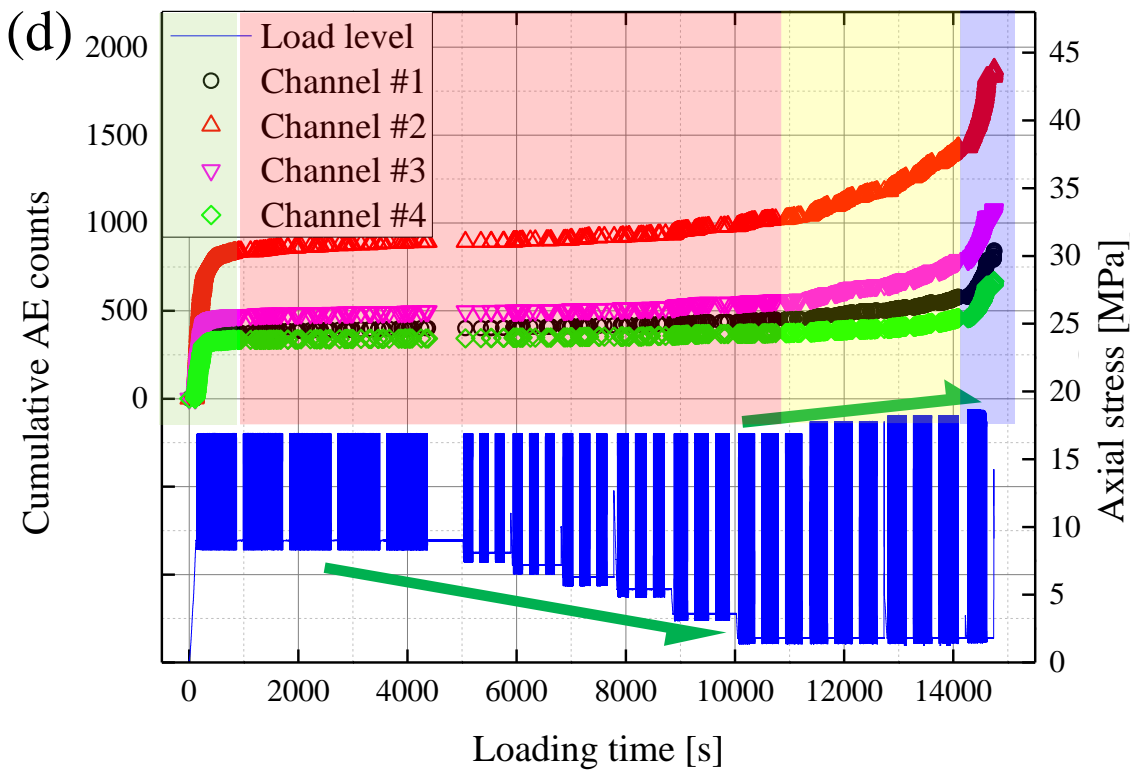
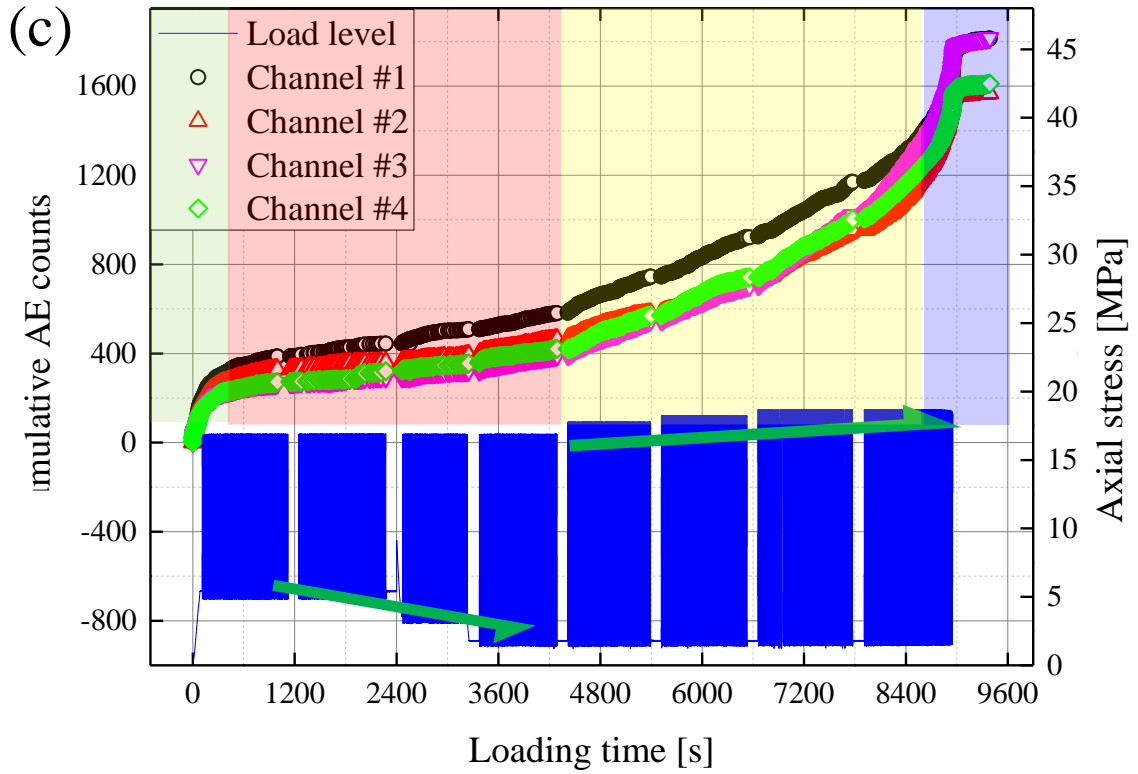
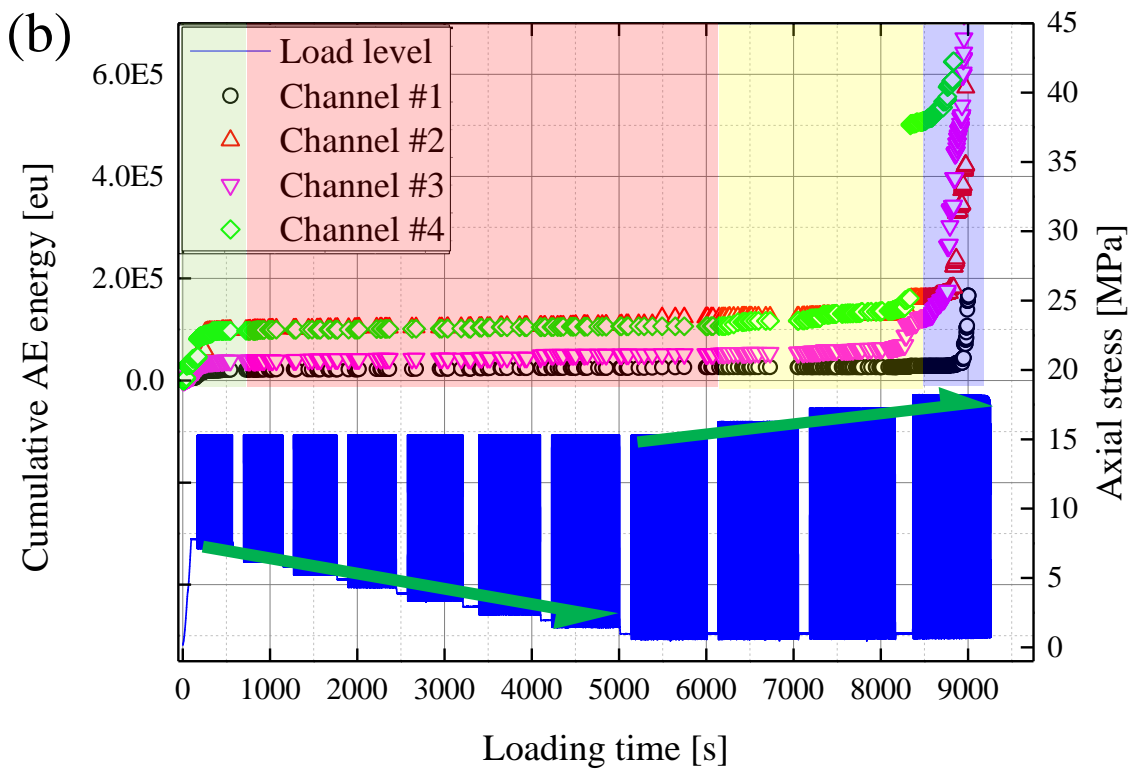
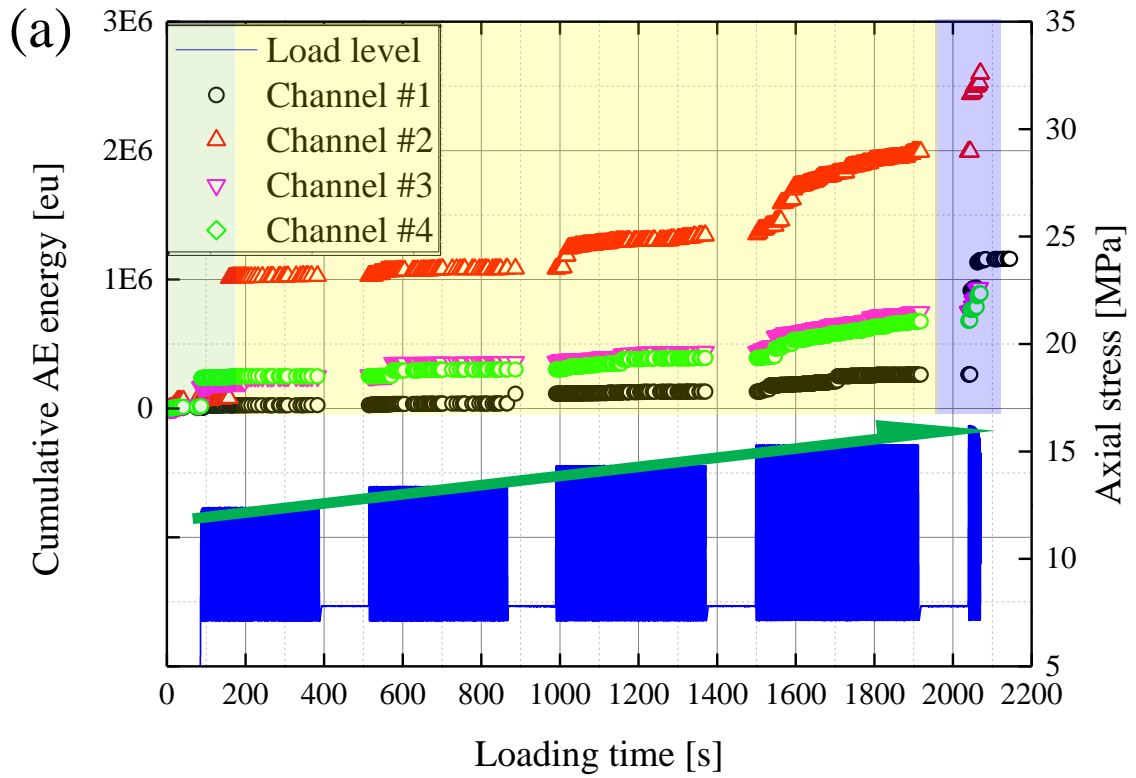


Fig. 3.13: Cumulative AE counts for (a) S2-13 (b) S2-14 (c) S1-10 (d) S1-8



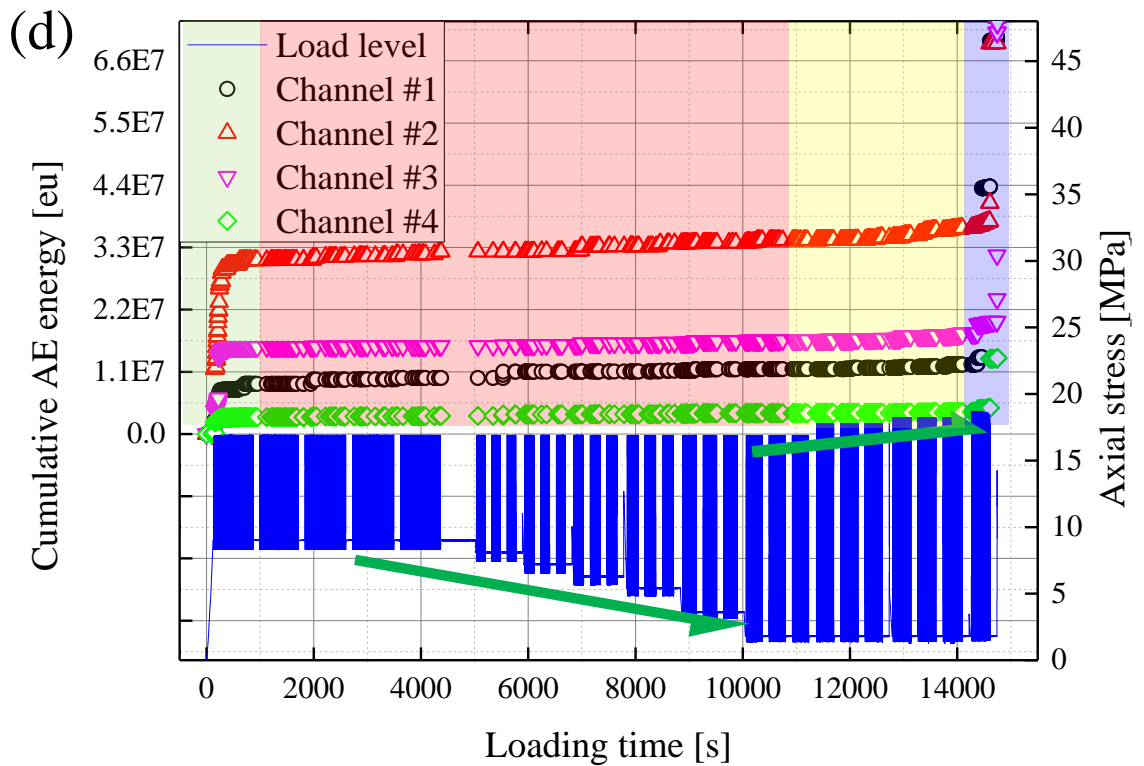
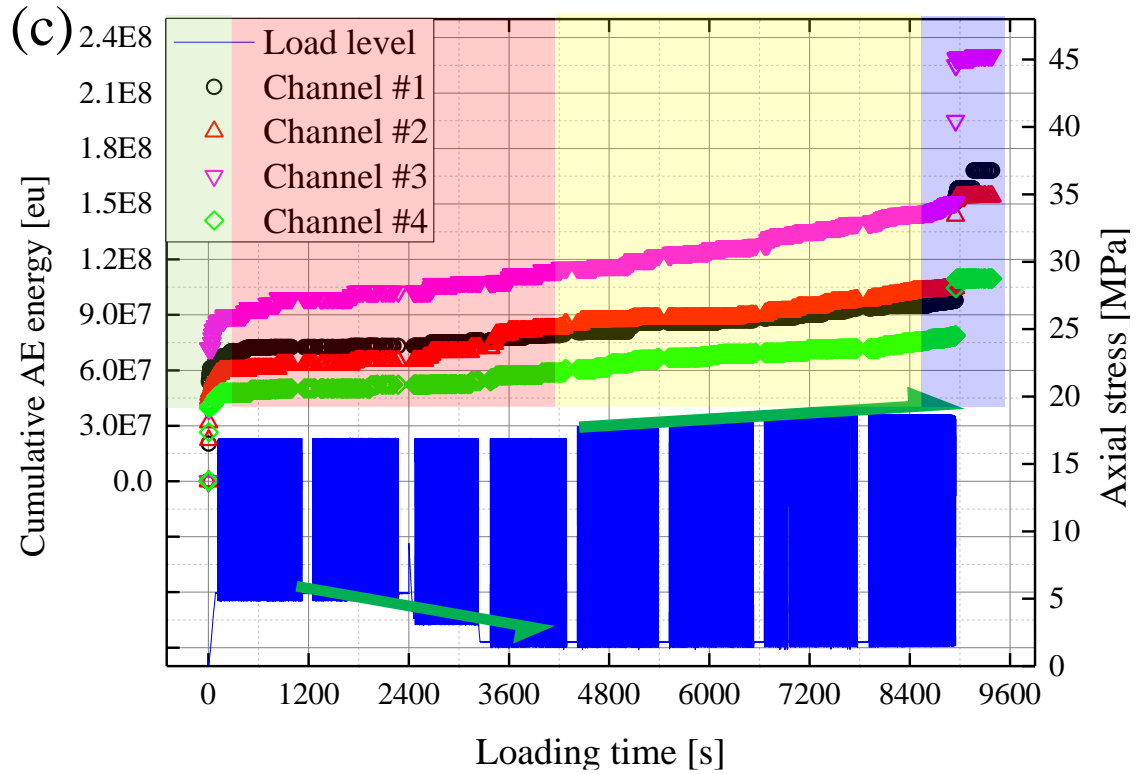


Fig. 3.14: Cumulative AE energy for (a) S2-13 (b) S2-14 (c) S1-10 (d) S1-8

3.4 Failure patterns of concrete specimens

Crack growth processes and failure patterns of brittle materials like concrete or rocks are different if they experience either monotonic or cyclic loading (Zhang & Zhao 2014; Cerfontaine & Collin 2018). It is found that under monotonic loading, almost all grains on the failure surface are highly cracked and failure pattern is brittle (Erarslan et al. 2014; Yang et al. 2015). Under cyclic loading, most grains are crack-free and failure develops mainly along grain boundaries. The failure patterns of concrete samples are shown in Fig. 3.15. The eight samples are categorized into four groups according to the loading strategies. The samples S2-15 and S2-16 (Group 1) are monotonically loaded with loading speed of 0.125 mm/min. The samples S1-6 and S1-7 (Group 2) are cyclically loaded, and both samples failed within only one cyclic loading stage. The samples S1-3 and S1-5 (Group 3) are cyclically loaded, and both samples failed after multi-level cyclic loading stages. During these stages, σ_{min} is fixed and σ_{max} is gradually increased. The samples S2-13 and S2-14 (Group 4) are cyclically loaded. These samples underwent two loading strategies. Note that the surface of samples of Group 4 are roughened to stick the strain gauges:

- σ_{max} is fixed and σ_{min} is gradually decreased
- σ_{min} is fixed and σ_{max} gradually increased.

From the viewpoint of mechanics, the failure of concrete or rocks subjected to external load, such as earthquakes or rock bursts, is connected with a rapid release of energy (Yin et al. 2004, 2008; Zhang & Zhuang 2011). Monotonic loading is characterized by dominant absorption of energy produced by external load. This will lead to macroscopic persistent cracks or sample splitting, see Fig. 3.15a. The samples S1-7 and S1-6 undergo 11 and 34 cycles, respectively, up to failure within only one cyclic loading stage. The low cycle number is caused by the higher level of σ_{max} which results in larger energy absorption in each cycle. Some persistent cracks can be observed in Fig. 3.15b and small concrete pieces are spalled from the sample. Compared to Group 1 and Group 2, the crack sizes observed in samples of Group 3 and Group 4 are much smaller, no persistent cracks are observed (see Fig. 3.15c and Fig. 3.15d). The samples of Group 3 and Group 4 experienced more than 600 loading cycles. The internal smaller cracks (micro-cracks) are evenly distributed over the whole sample. The axial and lateral strain at peak stress of the last cycle for the eight samples are shown in Fig. 3.16. The monotonically loaded samples show an obviously smaller axial strain (see Fig. 3.16a) and lateral strain (see Fig. 3.16b) than the cyclically loading samples. This illustrates that the unloading stages in cyclic loading enable the samples to experience larger axial and lateral strain than under monotonic loading. Thus, the unloading stages in cyclic loading can be beneficial to enhance the energy absorption and reduce the rapid release of energy typically leading to violent failure with macroscopic persistent cracks or sample splitting.

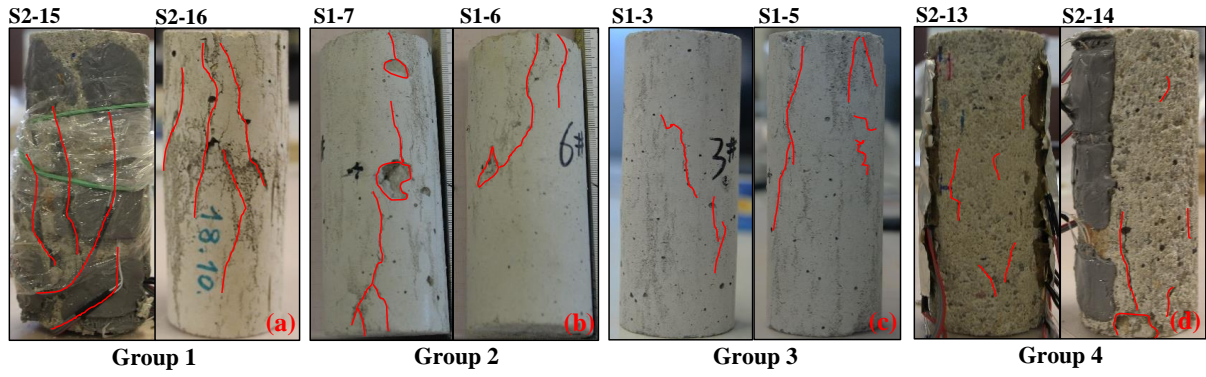


Fig. 3.15: Failure patterns of samples (a) Group 1 (b) Group 2 (c) Group 3 (d) Group 4

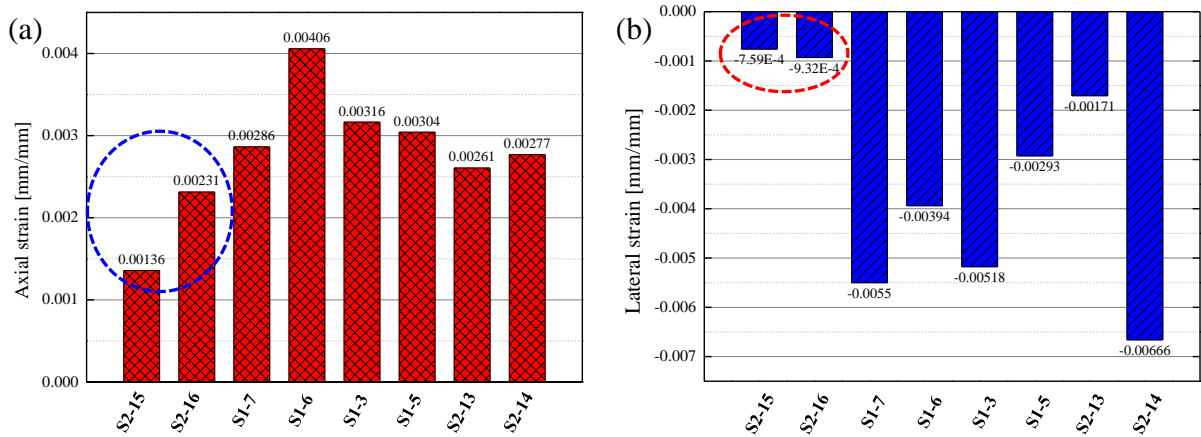


Fig. 3.16: (a) axial strain at peak stress of the last cycle (b) lateral strain at peak stress of the last cycle

4 References

- Aïtcin, P.C. (2003) The durability characteristics of high performance concrete: a review. *Cem Concr Compos* 25:409–420.
- Albert, W. (1838) Über Treibseile am Harz. *Arch fuer Mineral Geognosie, Bergbau und Hüttenkunde* 10:215–234.
- Allische, A. (2004) Damage model for fatigue loading of concrete. *Int J Fatigue* 26:915–921.
- Bagde, M.N. & Petroš, V. (2005a) Waveform effect on fatigue properties of intact sandstone in uniaxial cyclical loading. *Rock Mech Rock Eng* 38:169–196.
- Bagde, M.N. & Petroš, V. (2005b) Fatigue properties of intact sandstone samples subjected to dynamic uniaxial cyclical loading. *Int J Rock Mech Min Sci* 42:237–250.
- Bagde, M.N. & Petroš, V. (2009) Fatigue and dynamic energy behaviour of rock subjected to cyclical loading. *Int J Rock Mech Min Sci* 46:200–209.
- Baluch, M.H., Al-Gadhib, A.H., Khan, A.R. & Shaalan, A. (2003) CDM model for residual strength of concrete under cyclic compression. *Cem Concr Compos* 25:503–512.
- Bernard, S., Balla, V.K., Bose, S. & Bandyopadhyay, A. (2011) Rotating bending fatigue response of laser processed porous NiTi alloy. *Mater Sci Eng C* 31:815–820.
- Boukpeti, N., Lehane, B. & Carraro, J.A.H. (2014) Strain accumulation procedure during staged cyclic loading of carbonate sediments. In: *Proceedings of the ASME 2014 33rd International Conference on Ocean, Offshore and Arctic Engineering*. San Francisco, p 23692
- Bumanis, G., Dembovska, L., Korjakins, A. & Bajare, D. (2018) Applicability of freeze-thaw resistance testing methods for high strength concrete at extreme $-52.5\text{ }^{\circ}\text{C}$ and standard $-18\text{ }^{\circ}\text{C}$ testing conditions. *Case Stud Constr Mater* 8:139–149.
- Cerfontaine, B. & Collin, F. (2018) Cyclic and fatigue behaviour of rock materials: review, interpretation and research perspectives. *Rock Mech Rock Eng* 51:391–414.
- Chen, T.C., Yeung, M.R. & Mori, N. (2004) Effect of water saturation on deterioration of welded tuff due to freeze-thaw action. *Cold Reg Sci Technol* 38:127–136.
- Chen, W. & Konietzky, H. (2014) Simulation of heterogeneity, creep, damage and lifetime for loaded brittle rocks. *Tectonophysics* 633:164–175.
- Chen, X., Huang, Y., Chen, C., et al. (2017) Experimental study and analytical modeling on hysteresis behavior of plain concrete in uniaxial cyclic tension. *Int J Fatigue* 96:261–269.
- Dang, W., Konietzky, H. & Frühwirt, T. (2017) Direct shear behavior of planar joints under cyclic normal load conditions: effect of different cyclic normal force amplitudes. *Rock Mech. Rock Eng.* 50:3101–3107.
- Dang, W., Konietzky, H. & Frühwirt, T. (2016) Direct shear behavior of a plane joint under dynamic normal load (DNL) conditions. *Eng Geol* 213:133–141.
- Dattoma, V. & Giancane, S. (2013) Evaluation of energy of fatigue damage into GFRC through digital image correlation and thermography. *Compos Part B Eng* 47:283–289.
- Erarslan, N., Alehossein, H. & Williams, D.J. (2014) Tensile fracture strength of brisbane

- tuff by static and cyclic loading tests. *Rock Mech Rock Eng* 47:1135–1151.
- Fairhurst, C. (1964) On the validity of the 'Brazilian' test for brittle materials. *Int J Rock Mech Min Sci Geomech Abstr* 1:535–546.
- Fan, X., Hu, S., Lu, J. & Wei, C. (2016) Acoustic emission properties of concrete on dynamic tensile test. *Constr Build Mater* 114:66–75.
- Fathi, A., Moradian, Z., Rivard, P. & Ballivy, G. (2016) Shear mechanism of rock joints under pre-peak cyclic loading condition. *Int J Rock Mech Min Sci* 83:197–210.
- Ge, X., Jiang, Y., Lu, R. & Ren, J. (2003) Testing study on fatigue deformation law of rock under cyclic loading. *Chinese J Rock Mech Eng* 22:1591–1585.
- Ge, X. & Lu, Y. (1992) tudy on fatigue damage and irreversible deformation law of rock under cyclic. *Chinese J Geotechnical Eng* 14:56–60.
- Goel, S. Singh, S.P. & Singh, P. (2012) Flexural fatigue strength and failure probability of Self Compacting Fibre Reinforced Concrete beams. *Eng Struct* 40:131–140.
- Grossi, C.M., Brimblecombe, P. & Harris I. (2007) Predicting long term freeze–thaw risks on Europe built heritage and archaeological sites in a changing climate. *Sci Total Environ* 377:273–281.
- Hanif, A., Usman, M., Lu, Z., et al. (2018) Flexural fatigue behavior of thin laminated cementitious composites incorporating cenosphere fillers. *Mater Des* 140:267–277.
- He, J., Pan, J. & Wang, A. (2014) Acoustic emission characteristic of coal specimen under triaxial cyclic loading and unloading. *J China Coal Soc* 39:84–90.
- He, M., Huang, B., Zhu, C. et al. (2018) Energy dissipation-based method for fatigue life prediction of rock salt. *Rock Mech Rock Eng* 51:1447–1455.
- Henry, H.A.L. (2007) Soil freeze–thaw cycle experiments: Trends, methodological weaknesses and suggested improvements. *Soil Biol Biochem* 39:977–986.
- Hu, X., Lu, Q., Xu, Z. et al. (2018) Compressive stress-strain relation of recycled aggregate concrete under cyclic loading. *Constr Build Mater* 193:72–83.
- Hudson, J.A., Brown, E.T. & Rummel, F. (1972) The controlled failure of rock discs and rings loaded in diametral compression. *Int J Rock Mech Min Sci Geomech Abstr* 9:241–248.
- Isailović, I. & Wistuba, M.P. (2018) Asphalt mixture layers' interface bonding properties under monotonic and cyclic loading. *Constr Build Mater* 168:590–597.
- ISRM (1978) Suggested methods for determining tensile strength of rock materials. *Int J Rock Mech Min Sci Geomech Abstr* 15:99–103.
- Jia, C., Xu, W., Wang, R. et al. (2018) Characterization of the deformation behavior of fine-grained sandstone by triaxial cyclic loading. *Constr Build Mater* 162:113–123.
- Jia, H., Wang, E., Song, D. et al. (2019) Precursory changes in wave velocity for coal and rock samples under cyclic loading. *Results Phys* 12:432–434.
- Jiang, F., Liu, R. & Zhang, D. (1994) A fatigue damage function based on energy analysis. *J Harbin Eng Univ* 15:25–30.
- Jing, L., Stephansson, O. & Nordlund, E. (1993) Study of rock joints under cyclic loading conditions. *Rock Mech Rock Eng* 26:215–232.

- Khanlari, G. & Abdilor, Y. (2015) Influence of wet-dry, freeze-thaw, and heat-cool cycles on the physical and mechanical properties of upper red sandstones in central Iran. *Bull Eng Geol Environ* 74:1287–1300.
- Kim, J., Son, S., Rye, T. & Soriano, G. (2015) Effects of cyclic shear stress and average shear stress on the cyclic loading failure of marine silty sand. *Lowl Technol Int* 17:19–26.
- Le, K.N. & Ghayoomi, M. (2017) Cyclic direct simple shear test to measure strain-dependent dynamic properties of unsaturated sand. *Geotech Test J* 40:381–395.
- Lee, H.-J., Daniel, J.S. & Richard, K.Y. (2000) Continuum damage mechanics-based fatigue model of asphalt concrete. *J Mater Civ Eng* 12:105–112.
- Lei, D., Zhang, P., He, J. et al. (2017) Fatigue life prediction method of concrete based on energy dissipation. *Constr Build Mater* 145:419–425.
- Leng, J., Liao, C., Ye, G. & Jeng, D.-S. (2018) Laboratory study for soil structure effect on marine clay response subjected to cyclic loads. *Ocean Eng* 147:45–50.
- Li, D., Wang, E., Kong, X. et al. (2019) Damage precursor of construction rocks under uniaxial cyclic loading tests analyzed by acoustic emission. *Constr Build Mater* 206:169–178.
- Li, D. & Wong, L.N.Y. (2013) The Brazilian disc test for rock mechanics applications: review and new insights. *Rock Mech Rock Eng* 46:269–287.
- Liu, E. & He, S. (2012) Effects of cyclic dynamic loading on the mechanical properties of intact rock samples under confining pressure conditions. *Eng Geol* 125:81–91.
- Liu, E., He, S., Xue, X. & Xu, J. (2011) Dynamic properties of intact rock samples subjected to cyclic loading under confining pressure conditions. *Rock Mech Rock Eng* 44:629–634.
- Liu, X., Dai, F., Zhang, R. & Liu, J. (2015) Static and dynamic uniaxial compression tests on coal rock considering the bedding directivity. *Environ Earth Sci* 73:5933–5949.
- Liu, Y., Dai, F., Xu, N. et al. (2018) Experimental and numerical investigation on the tensile fatigue properties of rocks using the cyclic flattened Brazilian disc method. *Soil Dyn Earthq Eng* 105:68–82.
- Ma, L., Liu, X., Wang, M. et al. (2013) Experimental investigation of the mechanical properties of rock salt under triaxial cyclic loading. *Int J Rock Mech Min Sci* 62:34–41.
- Minto, T.A., de Oliveira, V.M.C.A. & Voorwald HJC (2017) Plasma immersion ion implantation: Influence on the rotating bending fatigue strength of AA 7050-T7451 aluminum alloy. *Int J Fatigue* 103:17–27.
- Naderi, M. & Khonsari, M.M. (2013) On the role of damage energy in the fatigue degradation characterization of a composite laminate. *Compos Part B Eng* 45:528–537.
- Oliveira, P.J.V., Correia, A.A.S. & Cajada, J.C.A. (2018) Effect of the type of soil on the cyclic behaviour of chemically stabilised soils unreinforced and reinforced with polypropylene fibres. *Soil Dyn Earthq Eng* 115:336–343.
- Oneschkow, N. (2016) Fatigue behaviour of high-strength concrete with respect to strain and stiffness. *Int J Fatigue* 87:38–49.

- Özbek, A. (2014) Investigation of the effects of wetting-drying and freezing-thawing cycles on some physical and mechanical properties of selected ignimbrites. *Bull Eng Geol Environ* 73:595–609.
- Özdeş, H., Tiryakioğlu, M. & Eason, P.D. (2017) On estimating axial high cycle fatigue behavior by rotating beam fatigue testing: Application to A356 aluminum alloy castings. *Mater Sci Eng A* 697:95–100.
- Paris, P., Director, A. & Erdogan, F. (1963) A critical analysis of crack propagation laws. *J Basic Eng* 85:528–533.
- Polder, R.B. & Peelen, W.H.A. (2002) Characterisation of chloride transport and reinforcement corrosion in concrete under cyclic wetting and drying by electrical resistivity. *Cem Concr Compos* 24:427–435.
- Qi, J., Vermeer, P.A. & Cheng, G. (2006) A review of the influence of freeze-thaw cycles on soil geotechnical properties. *Permafr Periglac Process* 17:245–252.
- Ramakrishnan, V., Malhotra, V.M. & Langley, W.S. (2005) Comparative evaluation of flexural fatigue behavior of high-volume fly ash and plain concrete. In: *SP-229: Qlty of Conc Struct and Recent Advances in Conc Matls & Testing: An Intl Conf Honoring V. Mohan Malhotra*. pp 351–368
- Rao, M.V.M.S. & Ramana, Y.V. (1992) A study of progressive failure of rock under cyclic loading by ultrasonic and AE monitoring techniques. *Rock Mech Rock Eng* 25:237–251.
- Reinhardt, H.W. & Cornelissen, H.A.W. (1984) Post-peak cyclic behaviour of concrete in uniaxial tensile and alternating tensile and compressive loading. *Cem Concr Res* 14:263–270.
- Schmidtko, R.H. & Lajtai, E.Z. (1985) The long-term strength of lac du bonnet granite. *Int J Rock Mech Min Sci Geomech Abstr* 22:461–465.
- Schütz, W. (1996) A history of fatigue. *Eng. Fract. Mech.* 54:263–300.
- Shadman, M. & Ziari, H. (2017) Laboratory evaluation of fatigue life characteristics of polymer modified porous asphalt: A dissipated energy approach. *Constr Build Mater* 138:434–440.
- Shen, S., Airey, G.D., Carpenter, S.H. & Huang, H. (2006) A dissipated energy approach to fatigue evaluation. *Road Mater Pavement Des* 7:47–69.
- Singh, S.P. & Kaushik, S.K. (2003) Fatigue strength of steel fibre reinforced concrete in flexure. *Cem Concr Compos* 25:779–786.
- Singh, S.P. & Sharma, U.K. (2007) Flexural fatigue strength of steel fibrous concrete beams. *Adv Struct Eng* 10:197–207.
- Sohel, K.M.A., Al-Jabri, K., Zhang, M.H. & Liew, J.Y.R. (2018) Flexural fatigue behavior of ultra-lightweight cement composite and high strength lightweight aggregate concrete. *Constr Build Mater* 173:90–100.
- Song, Z., Frühwirth, T. & Konietzky, H. (2018) Characteristics of dissipated energy of concrete subjected to cyclic loading. *Constr Build Mater* 168:47–60.
- Song, Z., Konietzky, H. & Frühwirth, T. (2019) Hysteresis and dynamic response features of concrete exposed to repeated multilevel compressive loading. *J Mater Civ Eng* 31:04019066.

- Sumner, P.D. & Loubser, M.J. (2008) Experimental sandstone weathering using different wetting and drying moisture amplitudes. *Earth Surf Process Landforms* 33:985–990. doi: 10.1002/esp.1586
- Swab, J.J., Yu, J., Gamble, R. & Kilczewski, S. (2011) Analysis of the diametral compression method for determining the tensile strength of transparent magnesium aluminate spinel. *Int J Fract* 172:187–192.
- Tan, X., Chen, W., Yang, J. & Cao, J. (2011) Laboratory investigations on the mechanical properties degradation of granite under freeze–thaw cycles. *Cold Reg Sci Technol* 68:130–138.
- Tarefder, R.A., Bateman, D. & Swamy, A.K. (2013) Comparison of fatigue failure criterion in flexural fatigue test. *Int J Fatigue* 55:213–219.
- Tepfers, R., Hedberg, B. & Szczekocki, G. (1984) Absorption of energy in fatigue loading of plain concrete. *Matériaux Constr* 17:59–64.
- Tong, X., Wang, D. & Xu, H. (1989) Investigation of cyclic hysteresis energy in fatigue failure process. *Int J Fatigue* 11:353–359.
- Vicentini, D., Crocombe, A., Barroso, A. et al. (2014) Fatigue crack initiation and damage characterization in Brazilian test specimens for adhesive joints. *J Adhes Sci Technol* 28:1418–1431.
- Wang, D., Ma, W., Niu, Y. et al. (2007) Effects of cyclic freezing and thawing on mechanical properties of Qinghai–Tibet clay. *Cold Reg Sci Technol* 48:34–43.
- Wang, Q. & Xing, L. (1999) Determination of fracture toughness K_{IC} by using the flattened Brazilian disk specimen for rocks. *Eng Fract Mech* 64:193–201.
- Wang, Q.Z., Jia, X.M., Kou, S.Q. et al. (2004) The flattened Brazilian disc specimen used for testing elastic modulus, tensile strength and fracture toughness of brittle rocks: analytical and numerical results. *Int J Rock Mech Min Sci* 41:245–253.
- Wang, Y., Wang, C. & Bahia, H. (2017) Comparison of the fatigue failure behaviour for asphalt binder using both cyclic and monotonic loading modes. *Constr Build Mater* 151:767–774.
- Wöhler, A. (1870) Über die Festigkeitsversuche mit Eisen und Stahl. *Zeitschrift für Bauwesen* 20:73–106.
- Xiao, J.-Q., Ding, D.-X., Jiang, F.-L. & Xu, G. (2010) Fatigue damage variable and evolution of rock subjected to cyclic loading. *Int J Rock Mech Min Sci* 47:461–468.
- Xiao, J.-Q., Ding, D.-X., Xu, G. & Jiang, F.-L. (2009) Inverted S-shaped model for nonlinear fatigue damage of rock. *Int J Rock Mech Min Sci* 46:643–648.
- Xie, H., Ju, Y. & Li, L. (2005) Criteria for strength and structural failure of rocks based on energy dissipation and energy release principles. *Chinese J Rock Mech Eng* 24:3003–3010.
- Xie, H., Peng, R. & Ju, Y. (2004) Energy dissipation of rock deformation and fracture. *Chinese J Rock Mech Eng* 23:3565–3570.
- Xu, J. (2016) *Mechanics of fatigue*. Science Press, Beijing
- Xu, J., Tang, Y. & Zhou, J. (2017) Effect of drying-wetting cycles on aggregate breakdown for yellow-brown earths in karst areas. *Geoenvironmental Disasters* 4:20.

- Xu, T., Zhou, G., Heap, M.J. et al. (2018) The modeling of time-dependent deformation and fracturing of brittle rocks under varying confining and pore pressures. *Rock Mech Rock Eng* 51:3241–3263.
- Yassini, E., Mirzaei, M., Alimi, A. & Rahaeifard, M. (2016) Investigation of the fatigue behavior of adhesive bonding of the lithium disilicate glass ceramic with three resin cements using rotating fatigue method. *J Mech Behav Biomed Mater* 61:62–69.
- Zhang, S., Lai, Y., Zhang, X. et al. (2004) Study on the damage propagation of surrounding rock from a cold-region tunnel under freeze–thaw cycle condition. *Tunn Undergr Sp Technol* 19:295–302.
- Zhao, C., Koseki, J. & Sasaki, T. (2018) Image based local deformation measurement of saturated sand specimen in undrained cyclic triaxial tests. *Soils Found* 58:1313–1325.
- Zhou, Z., Cai, X., Chen, L. et al. (2017) Influence of cyclic wetting and drying on physical and dynamic compressive properties of sandstone. *Eng Geol* 220:1–12.